Pulse-based ISAC: Data Recovery and Ranging Estimation for Multi-Path Fading Channels

Shusen Cai, Li Chen *Senior Member IEEE*, Yunfei Chen *Senior Member IEEE*, Huarui Yin *Member IEEE*, and Weidong Wang

Abstract

Pulse-based integrated sensing and communication (ISAC) systems have the advantages of high ranging resolution and strong resistance to self-interference, compared with continuous wave (CW) based systems. However, for pulse-based ISAC systems, multi-path channels pose various challenges to data recovery and ranging by providing diversity gain for data recovery but incurring the interference to the identification of the first path in ranging. In this paper, we design a pulse-based ISAC receiver for multi-path channels. The designed receiver can obtain the diversity gain by correlating the received signal with the estimated template signal. Meanwhile, it can detect the arrival of the first path by using a threshold detection method based on a constant false alarm rate (CFAR). Furthermore, we extend the pulse-based ISAC design to a low-resolution analog-to-digital converter (ADC) scenario. A low-cost receiver design is provided for the pulse-based ISAC system that can recover data and estimate range simultaneously considering the non-linear effect caused by the low-resolution ADC. Simulation results show that compared with the generalized maximum likelihood (GML) based receiver, the proposed full-resolution pulse-based ISAC receiver has 1dB signal-to-noise ratio (SNR) loss in bit error rate (BER) and almost the same mean squared error (MSE) performance with the significantly reduced computational complexity. Also, compared with the full-resolution ISAC receiver, the ISAC receiver with 3-level quantization incurs only 0.8dB SNR loss in BER and 1dB SNR loss in MSE.

Index Terms

Data recovery, low-resolution ADC, ISAC, multi-path channel, pulse-based, ranging estimation.

Shusen Cai, Li Chen, Huarui Yin and Weidong Wang are with the Department of Electronic Engineering and Information Science, University of Science and Technology of China, Hefei 230027, Anhui, China (e-mail: cssemail@mail.ustc.edu.cn; chenli87@ustc.edu.cn; yhr@ustc.edu.cn; wdwang@ustc.edu.cn).

Yunfei Chen is with the Department of Engineering, University of Durham, Durham DH1 3LE, U.K. (e-mail: yunfei.chen@durham.ac.uk).

I. INTRODUCTION

Integrated sensing and communication (ISAC) has been a promising solution to the spectrum scarcity problem [1]–[4]. It can combine the functionalities of communication and sensing in a single system by sharing the same resources, including waveform, hardware, signal processing. To satisfy the growing demand for sensing in wireless communication systems, such as vehicle to everything (V2X) and industrial internet of thing (IoT), ISAC systems should not only keep high-quality wireless communication, but also have high-accuracy sensing capability.

Based on the used signal waveforms, ISAC systems can be mainly divided into continuous wave (CW) based ISAC systems and pulse-based ISAC systems. CW-based ISAC systems transmit signals constantly or only with a very short guard interval, and listen to echo signals or response signals simultaneously, while pulse-based ISAC systems adopt pulsed signals with low duty cycle, and the silent time (i.e. the time out of pulse duration) is usually used for waiting echo signals or response signals [1], [2]. In CW-based ISAC systems, the receivers can acquire the sensing information from the transmitted signal typically covering a large range of frequencies. Frequency modulated carrier wave (FMCW) is a traditional CW sensing signal, and it has been studied in the context of ISAC [5], [6]. In order to be used for both communication and sensing, FMCW has be multiplexed with or modulated by communication signals, such as frequency index modulation [5] and index modulation [6]. In addition to FMCW, orthogonal frequency-division multiplexing (OFDM) wave has also been adopted by CW-based ISAC systems [7]–[13]. In [7], the delay and Doppler estimation based on OFDM was performed by using fast Fourier transform (FFT) and inverse fast Fourier transform (IFFT). This algorithm mitigated the impact of random communication symbols and decoupled the two estimation. In [8]–[10], OFDM-based ISAC systems were implemented by allocating orthogonal wireless resources in spectral and code domains, such that communication and sensing did not interfere with each other. To achieve the joint optimization of sensing and communication, the shared waveform design of OFDM-based ISAC has been studied in [11]–[13].

Although CW-based ISAC has the advantage of high spectral efficiency for communication, it has the disadvantage of low-resolution sensing. High-resolution target location and imaging often require pulse-based systems [14]. Also, self-interference is a serious issue for CW-based ISAC systems [1], [15], [16]. The full-duplex operation based on the self-interference cancellation scheme was proposed in [15], [16], but these schemes were unable to obtain perfect self-interference cancellation, and they suffered from extremely high computational complexity in digital domain.

Pulse-based sensing systems have been widely used for many sensing applications, such

as location [17]–[20], target detection [21], [22] and imaging [23]–[26]. For communication systems, pulsed signals also have the advantages of low power consumption, high safety and high resistance against the narrowband interference [27]–[29]. Many modulation technologies, such as index modulation [30] and enhanced pulse position modulation [31], have been proposed for the high spectral efficiency and the low bit error rate (BER) of pulse-based communication systems. In [27], the power limit of pulsed signals considering the interference in in-car communication was discussed. A multi-user interference (MUI) and inter-symbol interference (ISI) problem in pulse-based communication systems was considered and a deep learning (DL) based receiver was designed to suppress MUI and ISI in [32]. An important issue of deep learning approaches was that the channel statistics for off-line training and on-line testing were not the same. The channel mismatches reduced the performance of the DL-based receiver.

Most research works about pulsed-based ISAC systems have mainly focused on waveform or beamforming design [33]–[36]. The design of signal waveform or beamforming was usually modeled as an optimization problem for satisfying the demands of communication and sensing. Because of the contradicting performance indicators for communication and sensing, the key parameters of signal waveform or beamforming were obtained by making a tradeoff between communication and sensing. These works have obtained the optimal ISAC waveform or beamforming based on different criterions, but not concerned the received signal processing.

The receiver design of pulse-based ISAC systems has not been well studied to the best of our knowledge. The main challenge is the channel estimation in dense multi-path channels for post-processing. For communication, the energy of the ultra-short sub-nanosecond transmitted pulses spreads over a very large number of multi-path components. In order to collect sufficient signal energy, combining a large number of multi-path components is required. For sensing, multi-path components will overlap with or even mask the target component and hence make sensing difficult. Although the aforementioned pulse-based sensing and communication systems considered the effect of multi-path channels, the multi-path effects on communication and sensing were so different that these existing designs could not be used directly in pulse-based ISAC systems.

The pulse-based sensing systems mainly adopted pulse-Doppler signals to perceive the environment [21], [23], [24]. The signals reflecting from non-target scatters were considered as clutters and should be suppressed to achieve a high-quality ranging-Doppler (RD) map. The traditional pulse-based radio systems collected multi-path signals by energy detection (ED) [37]–[39]. The information of energy distribution acquired by ED was used for data recovery, but not suitable for accurate time of arrival (ToA) estimation because of limited time resolutions

TABLE I

THE SUMMARY OF LITERATURE REVIEW

work Feature	CW-based			Pulse-based				Our work
	[6]	[5], [7], [8]	[9]–[13]	[18], [26]	[19]–[25]	[33]–[36]	[41]–[43]	
ISAC	√	√	√				√	√
High-precision sensing				√	√	√	√	√
Imperfect CSI							√	√
Low-cost scheme	√			√		√		√
Received signal processing	√	√		√	√		√	√
Frame Structure Design							√	√

[40]. The high-speed sampling reception method is a promising solution with advantages of high precision ranging and flexible signal processing in digital domain [41]–[43]. In [41], [43], a transmitted reference pulse cluster (TRPC) based receiver was proposed for joint symbol and ToA estimation by using an iterative detection algorithm. The data blocks should be used to obtain the reference signal iteratively. In [42], a pulse-based ISAC receiver based on a generalized maximum likelihood (GML) method [44], [45] has been provided. Although GML was able to offer the whole parameter information of multi-path channels (i.e. delay and path gain), the iterative computations made the computational complexity of GML excessively high.

Another challenge comes from the quantization of pulsed signals. The large bandwidth of pulsed signals is beneficial for high-accuracy sensing but incurs a high cost of the full-resolution analog-to-digital converter (ADC) (i.e. 8 bits or more) with a high-speed sampling rate. For example, a ideal b-bit ADC with flash architecture contains $2^b - 1$ comparators and its power consumption increases exponentially with the number of quantization bits [46]. To reduce power consumption and hardware cost, low-resolution ADCs (i.e. 1-2 bits) are applied at the cost of the performance loss [47]–[51]. The use of the low-resolution ADCs complicates the digital signal processing of sensing and communication because of the discretization of signal levels, which makes the low-resolution receiver design challenging.

In this paper, we study a pulse-based ISAC system which uses a packet consisting of preamble frames (PF) part for data recovery and ranging estimation. We propose a full-resolution receiver designed for joint data recovery and ranging estimation in multi-path channels. The noiseless sampled received waveform is adopted as channel state information (CSI) and simply obtained by maximum likelihood estimation (MLE) criterion based on PF. Then, we model data recovery and ranging estimation as two hypothesis testing problems. The symbol detector for data recovery is designed to perform an inner product calculation with the estimated CSI for achieving the

diversity gain. Then, by reusing CSI, the estimator for ranging can detect the ToA of the returned packet by the threshold detection method based on Neyman-Pearson (NP) rule. Associated BER and Cramer-Rao lower bound (CRLB) expressions are provided. Considering the high cost of the high-speed full-resolution ADC, an ISAC receiver with the low-resolution ADC is proposed for low-cost design. To avoid infeasible non-linear calculations caused by discrete signal levels, we obtain the linear detectors of data recovery and ranging estimation from Taylor series expansions of the log-likelihood ratio (LLR), and associated BER and CRLB expressions are also provided. Finally, we analyze the optimization of some key parameters (i.e. quantization thresholds and PF length) and then propose the corresponding parameter design schemes. The simulation results verify the theoretical analysis of key parameters, show the impact of narrowband interference (NBI) and the correlation of sample points on the proposed ISAC systems, and offer the performance comparison between conventional receivers and our proposed receivers. Compared with the GML-based receiver, the proposed full-resolution ISAC receiver has about 1dB signal-to-noise ratio (SNR) loss in the same BER and near the same mean squared error (MSE) performance with the significantly reduced computational complexity. The performance loss caused by the low-resolution quantization is also provided. The 3-level ISAC receiver, for example, has about 0.8dB SNR gap compared with the full-resolution ISAC receiver in BER, and about 1dB SNR gap in MSE, which is exchanged for reducing the cost of the ADC. The main contributions of this paper are summarized as follows:

- **Full-resolution pulse-based ISAC receiver and performance:** Considering the different effects of the multi-path components on data recovery and ranging estimation, the proposed receiver can effectively obtain the diversity gain for data recovery, and estimate the delay of the first path for ranging estimation. The BER and CRLB are analyzed to assess their performances.

- **Low-cost low-resolution pulse-based ISAC receiver and performance:** To reduce the cost of high-speed full-resolution ADC, we propose a pulse-based ISAC receiver using a low-resolution ADC for low-cost design. The low-resolution receiver eliminates the non-linear effect on both data recovery and ranging estimation caused by discrete signal levels. The BER and CRLB are provided.

- **Key parameters analysis and design:** Based on the design of the above receivers, we analyze the effects of quantization thresholds and PF length on BER and CRLB. Then, the analytical expressions of the optimal quantization thresholds that minimize BER and CRLB are obtained, and the allocation method of PF length based on maximum data transmission capability is proposed.

The rest of the paper is organized as follows. In Section II, we will describe the ISAC system based on pulsed signals. In Sections III and IV, we will present the receiver design with the full-resolution and low-resolution ADC respectively, and analyze their BER and CRLB. The effect and design of PF length and quantization thresholds are discussed for the parameter optimization of the pulse-based ISAC receivers. Simulation results will be shown in Section V, followed by the conclusions in Section VI

Notations: a is a scalar, $\mathbf{a}$ is a vector, $\mathbf{A}$ is a matrix. $\mathbf{I}_a$ is an $a \times a$ identity matrix. $\mathbb{R}$ represents a real number field. $\mathbf{x} \sim \mathcal{CN}(\mathbf{a}, \mathbf{A})$ means that $\mathbf{x}$ obeys a Gaussian distribution with mean $\mathbf{a}$ and autocovariance matrix $\mathbf{A}$. $\mathrm{E}[\cdot]$ and $\mathrm{var}[\cdot]$ are the calculations of mathematical expectation and variance respectively, and $\mathrm{cov}(\mathbf{a})$ is the autocovariance matrix of the random vector $\mathbf{a}$. $(\cdot)^T$ is defined as the transpose of a matrix or a vector. $\mathrm{diag}\{\mathbf{a}\}$ represents a diagonal matrix whose diagonal elements are $\mathbf{a}$. $[a]$ is a rounding function which obtains the integer part of a. $f(t) * g(t)$ represents the convolution calculation of continuous functions $f(t)$ and $g(t)$, and $\langle \mathbf{a}, \mathbf{b} \rangle$ represents the inner product of vectors $\mathbf{a}$ and $\mathbf{b}$.

II. SYSTEM MODEL

Consider an ISAC system using pulsed signals, as illustrated in Fig. 1. The system has two ISAC nodes, which generalizes the typical applications in the dense multi-path propagation environment (e.g. indoor field or city block), like indoor communication and location, V2X, industrial IoT, etc. Assuming that the channels are reciprocal, Node A and Node B communicate with each other in packets, and estimate the distance by single-sided two-way ranging (SS-TWR) [52]. The distance between two nodes is denoted as $D = (T_{\mathrm{rd}} - T_{\mathrm{rp}})/2c$, where D is the distance between Node A and Node B, T_{rd} is the duration from sending out the transmitted packet to receiving the returned packet, T_{rp} is the fixed processing delay and c is the speed of light.

The packet is divided into data frames (DF) and PF. The PF consist of known pulses. From communication perspective, PF are used for obtaining CSI and DF are used for information exchange. From ranging perspective, CSI is reused for ranging. The length of PF and DF can be denoted as N_{p} and N_{d}, respectively.

Therefore, the transmitted pulsed signal of a packet can be given by

$$s(t) = \sum_{k_{\mathrm{p}}=0}^{N_{\mathrm{p}}-1} a_{k_{\mathrm{p}}} p(t - k_{\mathrm{p}} T_{\mathrm{s}}) + \sum_{k_{\mathrm{d}}=0}^{N_{\mathrm{d}}-1} b_{k_{\mathrm{d}}} p(t - N_{\mathrm{p}} T_{\mathrm{s}} - k_{\mathrm{d}} T_{\mathrm{s}}), \tag{1}$$

where $\mathbf{a} = [a_0, a_1, ..., a_{N_{\mathrm{p}}-1}]^T$ and $\mathbf{b} = [b_0, b_1, ..., b_{N_{\mathrm{d}}-1}]^T$ are transmitted symbol vectors of PF and DF respectively, $p(t)$ is the shaping pulse and T_{s} is the symbol duration. Note that k_{p} and k_{d} represents the k_{p}th symbol duration of preamble frames and the k_{d}th symbol duration of

data frames respectively. In addition, k is adopted for the whole packet which is comprised of preamble frames ($k \in [0, N_{\mathrm{p}} - 1]$) and data frames ($k \in [N_{\mathrm{p}}, N - 1]$). $N = N_{\mathrm{p}} + N_{\mathrm{d}}$ is the total number of symbols in the packet.

The multi-path channel is modeled as a linear time-invariant system with a finite impulse response which is given by

$$h(t) = \sum_{l=1}^{L} h_l \delta(t - \tau_l), \tag{2}$$

where h_l and τ_l are the gain and delay of the lth tap respectively. L is the number of paths in multi-path channels. Without loss of generality, we assume that $\tau_1 \leqslant \tau_2 \leqslant ... \leqslant \tau_L$. τ_1 is the ToA of the pulsed signal. The accurate ToA estimation of the returned packet is critical for a high-precision distance measurement. In a non line of sight (NLoS) environment, since the signals reflecting from scatters travel an extra distance compared to a line of sight (LoS) path, a positive bias called NLoS error is present in the distance measurement [53]. There have existed many NLoS identification and mitigation methods dealing with NLoS error [20], [54], [55]. For simplicity, we assume that the system operates in the LoS scenario.

At first, the transmitted signal is distorted by the multi-path channels and additive white Gaussian noise (AWGN), and then is filtered by a low-pass filter (LPF) of bandwidth B to eliminate out-of-band noise, Then, the filtered received signal is given by

$$r_{\mathrm{f}}(t) = \sum_{k_{\mathrm{p}}=0}^{N_{\mathrm{p}}-1} a_{k_{\mathrm{p}}} p_{\mathrm{f}}(t - k_{\mathrm{p}} T_{\mathrm{s}}) + \sum_{k_{\mathrm{d}}=0}^{N_{\mathrm{d}}-1} b_{k_{\mathrm{d}}} p_{\mathrm{f}}(t - N_{\mathrm{p}} T_{\mathrm{s}} - k_{\mathrm{d}} T_{\mathrm{s}}) + n(t), \tag{3}$$

where $p_{\mathrm{f}}(t) = p(t) * h(t) * h_{\mathrm{LPF}}(t)$ is the filtered pulse with the distortion resulting from the multi-path channels, $h_{\mathrm{LPF}}(t)$ is the impulse response of the LPF and $n(t)$ is the filtered noise with double-sided power spectral density $N_0/2$ limited in the frequency band $[B, -B]$. Assume that the symbol duration T_{s} is larger than the maximum channel delay so that ISI can be ignored.

After being filtered, $r_{\mathrm{f}}(t)$ should be sampled with sampling period T_{sam}, and then quantized by a full-resolution ADC for digital processing. Every symbol is sampled by $N_{\mathrm{s}} = [T_{\mathrm{s}}/T_{\mathrm{sam}}]$ points. The resultant of sampling can be a vector $\mathbf{r}$

$$\mathbf{r} = [\underbrace{r_{0,0}, ..., r_{N_{\mathrm{s}}-1,0}}_{\text{The first symbol}}, \underbrace{r_{0,1}, ..., r_{N_{\mathrm{s}}-1,1}}_{\text{The second symbol}}, ..., r_{N_{\mathrm{s}}-1,N-1}]^T, \tag{4}$$

where $r_{i,k}$ is the ith full-resolution sample point within the kth symbol duration of the packet. In order to facilitate the subsequent analysis, the vector $\mathbf{r}$ is reshaped as a full-resolution sample

point matrix $\mathbf{R} \in \mathbb{R}^{N_s \times N}$ according to different symbol durations, which is given by

$$\mathbf{R} = \mathbf{w}\mathbf{d}^T + \mathbf{N}$$

$$= \begin{bmatrix} r_{0,0} & \cdots & r_{0,N_p-1} & r_{0,N_p} & \cdots & r_{0,N-1} \\ r_{1,0} & \cdots & r_{1,N_p-1} & r_{1,N_p} & \cdots & r_{1,N-1} \\ \vdots & \ddots & \vdots & \vdots & \ddots & \vdots \\ r_{N_s-1,0} & \cdots & r_{N_s-1,N_p-1} & r_{N_s-1,N_p} & \cdots & r_{N_s-1,N-1} \end{bmatrix},$$

$$\underbrace{\qquad\qquad\qquad\qquad}_{\text{preamble frames: } \mathbf{R}_p} \underbrace{\qquad\qquad\qquad\qquad}_{\text{data frames: } \mathbf{R}_d}$$

(5)

where $\mathbf{w} = [w_0, w_1, ..., w_{N_s-1}]^T$ is the sample point vector of $p_f(t)$ being independent of k, $\mathbf{d}^T = [\mathbf{a}^T, \mathbf{b}^T]$ is the row symbol vector, and $\mathbf{N} \in \mathbb{R}^{N_s \times N}$ is a random matrix whose entries $n_{i,k}$ are independent identically distributed (i.i.d.) Gaussian random variables with zero mean and variance $\sigma_n^2 = N_0 B$. Furthermore, $\mathbf{R}$ can be divided into the PF sample point matrix $\mathbf{R}_p$ and the DF sample point matrix $\mathbf{R}_d$ whose entries are denoted as $r_p^{(i,k_p)}$ and $r_d^{(i,k_d)}$ respectively. $\mathbf{N}$ can also be divided into $\mathbf{N}_p$ and $\mathbf{N}_d$ in the same way, and their entries are denoted as $n_p^{(i,k_p)}$ and $n_d^{(i,k_d)}$ respectively.

Then, the PF sample point matrix $\mathbf{R}_p$ is used for channel estimation. After channel estimation, the ISAC receiver will use the DF sample point matrix $\mathbf{R}_d$ to recover the data. The results of the data decision is denoted as $\hat{\mathbf{b}} = [\hat{b}_0, \hat{b}_1, ..., \hat{b}_{N_d-1}]$. Simultaneously, the output of the channel estimation can be reused to estimate the distance D.

For the receiver design of the pulse-based ISAC system, the multi-path components lead to different problems for data recovery and ranging. For data recovery, multi-path components can be collected to achieve the diversity gain, while for ranging estimation, the first path will be identified in the presence of nuisance multi-path components.

III. RECEIVER DESIGN WITH FULL RESOLUTION

In this section, we propose a joint data recovery and ranging estimation method for multi-path channels using the full-resolution sampled signal. The block diagram of the post quantization processing part is illustrated in Fig. 2. We first propose a MLE method using PF for channel estimation. After the channel estimation, a symbol detector based on minimum BER criterion is designed for the data recovery of DF, and the BER of this symbol detector is provided in Section III-B. By reusing CSI, we design a ToA estimator based on threshold detection for ranging, and provide the CRLB of the ranging estimation in Section III-C. Finally, we analyze the effect of PF length N_p on both data recovery and ranging estimation, and propose an allocation method of time slots for pulse-based ISAC systems in Section III-D.
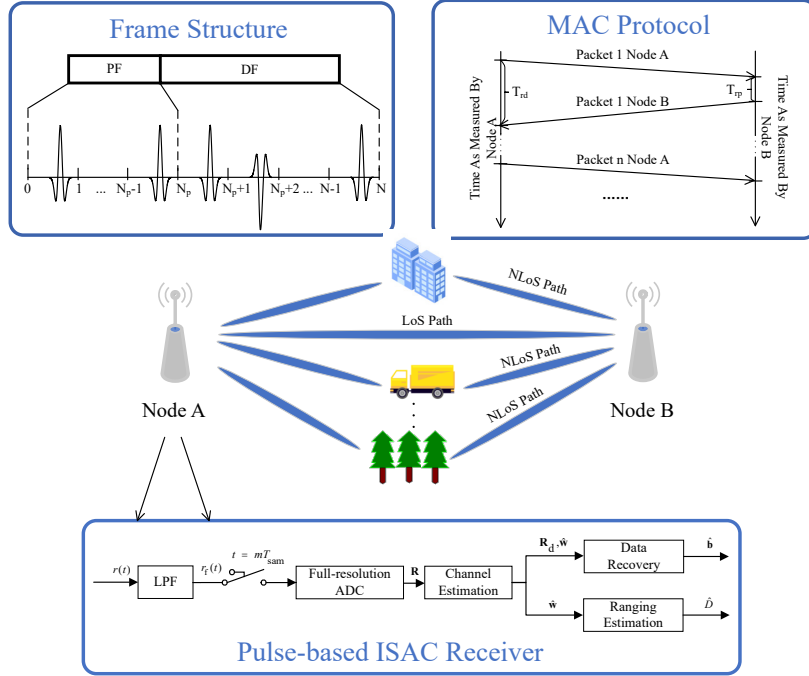
Fig. 1. System Model: a node-to-node ISAC system based on pulsed signals

A. Channel Estimation

Before the data recovery and the ranging estimation, we require the CSI of multi-path channels. From (5), it is noted that $w_i = \sum_{l=1}^{L} h_l p_{\mathrm{r}}((i+1)T_{\mathrm{sam}} - \tau_l)$ with $p_{\mathrm{r}}(t) = p(t) * h_{\mathrm{LPF}}(t)$ contains the parameters (i.e. delay and gain) of multi-path components. Only $\mathbf{w}$ is needed, which is estimated by using MLE criterion. The log-likelihood function of $\mathbf{w}$ is given by

$$L(\mathbf{R}_{\mathrm{p}}|\mathbf{a}, \mathbf{w}) = \sum_{i=0}^{N_{\mathrm{s}}-1} \sum_{k_{\mathrm{p}}=0}^{N_{\mathrm{p}}-1} \log f_{\mathrm{n}}(r_{\mathrm{p}}^{(i,k_{\mathrm{p}})} - a_{k_{\mathrm{p}}} w_i), \tag{6}$$

where $f_{\mathrm{n}}(\cdot)$ is the probability distribution function (PDF) of a Gaussian distribution with zero mean and variance σ_{n}^2. From (6), we can decompose the estimation of $\mathbf{w}$ into its entries w_i as

$$L(\mathbf{r}_{\mathrm{p,row}}^{(i)}|\mathbf{a}, w_i) = \sum_{k_{\mathrm{p}}=0}^{N_{\mathrm{p}}-1} \log f_{\mathrm{n}}(r_{\mathrm{p}}^{(i,k_{\mathrm{p}})} - a_{k_{\mathrm{p}}} w_i),$$

$$i = 0, 1, \ \ldots \ , N_{\mathrm{s}} - 1 \tag{7}$$

where $\mathbf{r}_{\mathrm{p,row}}^{(i)}$ denotes the ith row vector of $\mathbf{R}_{\mathrm{p}}$. Thus, the MLE of w_i is given by

$$\hat{w}_i = \arg\max_{w_i} L(\mathbf{r}_{\mathrm{p,row}}^{(i)}|\mathbf{a}, w_i)$$

$$= \frac{1}{N_{\mathrm{p}}} \sum_{k_{\mathrm{p}}=0}^{N_{\mathrm{p}}-1} a_{k_{\mathrm{p}}} r_{\mathrm{p}}^{(i,k_{\mathrm{p}})}, \quad i = 0, 1, \ \ldots \ , N_{\mathrm{s}} - 1 \tag{8}$$

where $\hat{\mathbf{w}} = [\hat{w}_0, \hat{w}_1, ..., \hat{w}_{N_\mathrm{s}-1}]^T$ is defined as the estimated CSI.

B. Data recovery

The data detection can be modeled as a hypothesis testing problem. We have two complementary hypotheses, $b_{k_\mathrm{d}} = 1$ or -1. That is,

$$
\begin{aligned}
\mathrm{H}_1 : r_\mathrm{d}^{(i,k_\mathrm{d})} &= w_i + n_\mathrm{d}^{(i,k_\mathrm{d})} \\
\mathrm{H}_0 : r_\mathrm{d}^{(i,k_\mathrm{d})} &= -w_i + n_\mathrm{d}^{(i,k_\mathrm{d})}.
\end{aligned}
\tag{9}
$$

Assuming that $p(\mathrm{H}_0) = p(\mathrm{H}_1) = \frac{1}{2}$, the log-likelihood ratio test (LLRT) of k_dth DF symbol based on minimum BER criterion is given by

$$
\begin{aligned}
\Lambda_\mathrm{d}(\mathbf{r}_\mathrm{d,col}^{(k_\mathrm{d})}) &= \sum_{i=0}^{N_\mathrm{s}-1} \log \frac{f_\mathrm{n}(r_\mathrm{d}^{(i,k_\mathrm{d})} - w_i)}{f_\mathrm{n}(r_\mathrm{d}^{(i,k_\mathrm{d})} + w_i)} \\
&= \frac{2}{\sigma_\mathrm{n}^2} \sum_{i=0}^{N_\mathrm{s}-1} w_i r_\mathrm{d}^{(i,k_\mathrm{d})} \underset{\mathrm{H}_0}{\overset{\mathrm{H}_1}{\gtrless}} 0,
\end{aligned}
\tag{10}
$$

where $\mathbf{r}_\mathrm{d,col}^{(k_\mathrm{d})}$ denotes the k_dth column vector of $\mathbf{R}_\mathrm{d}$. From (10), the symbol detector can be simplified as

$$
C_\mathrm{full}(\mathbf{r}_\mathrm{d,col}^{(k_\mathrm{d})}, \mathbf{w}) = \sum_{i=0}^{N_\mathrm{s}-1} w_i r_\mathrm{d}^{(i,k_\mathrm{d})} \underset{\mathrm{H}_0}{\overset{\mathrm{H}_1}{\gtrless}} 0.
\tag{11}
$$

Above all, the communication part of the post quantization processing shown in Fig. 2 consists of the channel estimation module and the data recovery module which are designed according to (8) and (11) respectively. The channel estimation module can be obtained by an correlator and a divider, and the data recovery module can be obtained by a correlator and a sign detector. With the input of $\mathbf{r}_\mathrm{d,col}^{(k_\mathrm{d})}$ and $\hat{\mathbf{w}}$, the correlator calculates the combined output $\sum_{i=0}^{N_\mathrm{s}-1} \hat{w}_i r_\mathrm{d}^{(i,k_\mathrm{d})}$. Then, the sign detector recovers the k_dth DF symbol by judging the polarity of $\sum_{i=0}^{N_\mathrm{s}-1} \hat{w}_i r_\mathrm{d}^{(i,k_\mathrm{d})}$.

Finally, the BER of the detector (11) considering the channel estimation error is given in Proposition 1.

Proposition 1 (BER of the full-resolution symbol detector). *Considering the channel estimation error and under the condition of large sample points $(N_\mathrm{p} \gg 1, N_\mathrm{s} \gg 1)$, the BER of $C_\mathrm{full}(\mathbf{r}_\mathrm{d,col}^{(k_\mathrm{d})}, \hat{\mathbf{w}})$ is given by [56]*

$$
P_\mathrm{e,full} = Q \left(\sqrt{\frac{2\mu\mathrm{SNR}}{1 + \frac{N_\mathrm{s}}{N_\mathrm{p}}(2\mu\mathrm{SNR})^{-1}}} \right),
\tag{12}
$$

where

$$
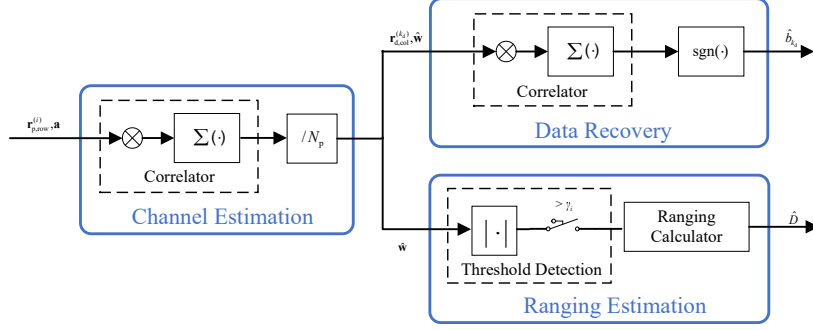\mathrm{SNR} = \frac{\int_0^{T_\mathrm{s}} p_\mathrm{f}^2(t)dt}{N_0}
\tag{13}
$$

Fig. 2. The block diagram of the post quantization processing part of the full-resolution ISAC receiver

is the SNR of $p_\mathrm{f}(t)$, μ is the constant ratio of the Nyquist sampling period $T_\mathrm{min} = \frac{1}{2B}$ to the sampling period T_sam and $Q(\cdot)$ denotes Gaussian Q function.

Proof. The proof is given in Appendix A. □

C. Ranging Estimation

As mentioned in Section II, only T_rd is unknown for ranging, which transforms the ranging estimation into the ToA estimation. Using PF, we propose a threshold detection method using LLRT which can be built on the estimated CSI (i.e. the MLE of $\mathbf{w}$). At first, the ToA estimation can be modeled as a signal detection problem

$$
\begin{aligned}
\mathrm{H}_1 &: r_\mathrm{p}^{(i,k_\mathrm{p})} = a_{k_\mathrm{p}} w_i + n_\mathrm{p}^{(i,k_\mathrm{p})} \\
\mathrm{H}_0 &: r_\mathrm{p}^{(i,k_\mathrm{p})} = n_\mathrm{p}^{(i,k_\mathrm{p})}.
\end{aligned}
\tag{14}
$$

Given the PF symbol vector $\mathbf{a}$, the LLR of the ith sample point is evaluated as

$$
\begin{aligned}
\Lambda_\mathrm{r}(\mathbf{r}_\mathrm{p,row}^{(i)}) &= \sum_{k_\mathrm{p}=0}^{N_\mathrm{p}-1} \log \frac{f_\mathrm{n}(r_\mathrm{p}^{(i,k_\mathrm{p})} - a_{k_\mathrm{p}} w_i)}{f_\mathrm{n}(r_\mathrm{p}^{(i,k_\mathrm{p})})} \\
&= \frac{1}{\sigma_\mathrm{n}^2} \sum_{k_\mathrm{p}=0}^{N_\mathrm{p}-1} a_{k_\mathrm{p}} w_i r_\mathrm{p}^{(i,k_\mathrm{p})} - \frac{N_\mathrm{p} w_i^2}{2\sigma_\mathrm{n}^2},
\end{aligned}
\tag{15}
$$

where $\mathbf{r}_\mathrm{p,row}^{(i)}$ denotes the ith row vector of $\mathbf{R}_\mathrm{p}$. Note that the amplitude of w_i has no effect on the detection, but the polarity of w_i decides the direction of the one-sided test. By considering the polarity of w_i and eliminating the irrelevant variables, the signal detector can be given by

$$
R_\mathrm{full}(\mathbf{r}_\mathrm{p,row}^{(i)}, \mathbf{a}, w_i) = \mathrm{sgn}(w_i) \cdot \sum_{k_\mathrm{p}=0}^{N_\mathrm{p}-1} a_{k_\mathrm{p}} r_\mathrm{p}^{(i,k_\mathrm{p})} \underset{\mathrm{H}_0}{\overset{\mathrm{H}_1}{\gtrless}} \gamma_i,
\tag{16}
$$

where γ_i is the decision threshold at ith sample point. The threshold γ_i with a constant false alarm rate ϵ is designed according to NP rule [56], which is set to

$$\gamma_i = \Phi^{-1}(1-\epsilon)\sqrt{\text{var}[R_{\text{full}}(\mathbf{r}_{\text{p,row}}^{(i)}, \mathbf{a}, w_i)|\text{H}_0]} + \text{E}[R_{\text{full}}(\mathbf{r}_{\text{p,row}}^{(i)}, \mathbf{a}, w_i)|\text{H}_0], \qquad (17)$$

where $\Phi(\cdot)$ is the cumulative distribution function (CDF) of the standard normal distribution. The first sample point that exceeds the threshold will be judged as the signal arrival. Then, ToA is estimated by

$$\tau_1 = T_{\text{sam}}\min_i\{i|R_{\text{full}}(\mathbf{r}_{\text{p,row}}^{(i)}, \mathbf{a}, w_i) > \gamma_i\} - T_{\text{sam}}/2. \qquad (18)$$

Above all, the ranging part of the post quantization processing shown in Fig. 2 consists of the channel estimation module and the ranging estimation module which are designed according to (8) and (16) respectively. Note that the calculation of $R_{\text{full}}(\mathbf{r}_{\text{p,row}}^{(i)}, \mathbf{a}, \hat{w}_i)$ is equivalent to the MLE of $|w_i|$. Thus, the output of the channel estimation module can be reused for the threshold detection. Then, the result of the ToA estimation is adopted for distance measurement.

The accuracy of the ranging estimation depends on many factors: transmitted pulsed signal waveform, multi-path channel state, the number of PF pulses, etc. To assess the impact of different factors on the ranging estimation, we choose CRLB as the performance metric. The CRLB of D is given in Proposition 2.

Proposition 2 (CRLB of D with full resolution)**.** *Because D is in a linear relationship with τ_1, the CRLB of D is equivalent to the CRLB of τ_1 multiplied by a constant c^2. Thus, we can evaluate the CRLB of D as*

$$\text{CRLB}_{D,\text{full}} = \frac{c^2}{8\pi^2(1-\eta)N_{\text{p}}\beta^2\mu\text{SNR}_{\text{p}}}, \qquad (19)$$

where

$$\text{SNR}_{\text{p}} = \frac{\int_{-\infty}^{+\infty} h_0^2 |P_{\text{r}}(f)^2|df}{N_0} \qquad (20)$$

and

$$\beta^2 = \frac{\int_{-\infty}^{+\infty} f^2 \cdot |P_{\text{r}}(f)^2|df}{\int_{-\infty}^{+\infty} |P_{\text{r}}(f)^2|df} \qquad (21)$$

are the SNR of the first path and the effective bandwidth of the filtered shaping pulse $p_{\text{r}}(t) = p(t) * h_{\text{LPF}}(t)$ respectively, $P_{\text{r}}(f)$ is the Fourier transform of $p_{\text{r}}(t)$ and $\eta \in [0,1]$ represents the overlapping coefficient caused by multi-path components (except the first path).
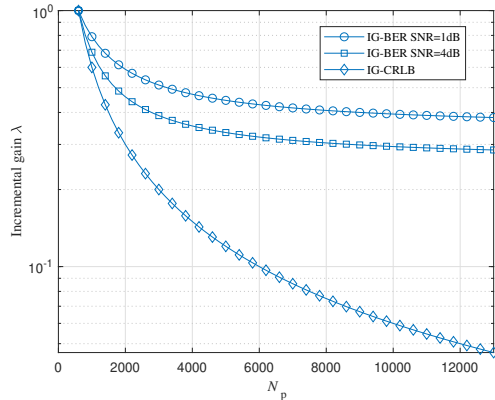
Proof. The proof is given in Appendix B. $\qquad\qquad\qquad\qquad\qquad\qquad\qquad\qquad\qquad\square$

Fig. 3. Analytical $\lambda(N_\mathrm{p})$ of the full-resolution ISAC receiver at various N_p and SNRs

Remark 1 (The effect of the multi-path overlapping). *As mentioned in Appendix B, η is a coefficient which describes the effect of the other paths on the estimation of the first path delay (i.e. τ_1). When the first path signal does not overlap with the other paths, $\eta = 0$. It means that we hope to reduce or eliminate the performance loss caused by irrelevant multi-path components in the ranging estimation. On the contrary, multi-path components are beneficial for the data recovery, which are considered as the copies of the transmitted signal and bring the extra gain of SNR.*

D. PF Length Design

Because the size of a packet is limited, the appropriate allocation of time slots for DF and PF is critical. As in (12) and (19), the increase of PF length N_p will reduce the BER and CRLB of the ISAC receiver, but decrease the DF length N_d. Thus, choosing an appropriate N_p is a key step of making a tradeoff among data transmission capacity, BER and CRLB.

At first, we study the effect of N_p on the data recovery and the ranging estimation. Some interesting properties can be obtained from (12) and (19). We consider a ISAC system with the initial PF length $N_\mathrm{p,int}$. For the ranging estimation, when $N_\mathrm{p,int}$ is increased by j times, CRLB will be decreased by j times. However, for the data recovery, the incremental gain of N_p is limited. Although $P_\mathrm{e,full}(N_\mathrm{p})$ increases monotonically with N_p, its growth rate decreases monotonically with N_p and $\lim_{N_\mathrm{p} \to +\infty} P_\mathrm{e,full}(N_\mathrm{p}) = Q(\sqrt{2\mu\mathrm{SNR}})$. When $N_\mathrm{p,int}$ is small, the increase of N_p will significantly reduce BER, but when $N_\mathrm{p,int}$ is large enough, the channel estimation error is so small that BER is almost not affected by N_p. In this case, the increase of

N_{p} is only beneficial to the ranging estimation and harmful to the data recovery because of the reduction of spectral efficiency.

In Fig. 3, we show the analytical results of BER and CRLB at various N_{p} and SNR. $N_{\mathrm{p,int}}$ is initialized to 600. The symbol duration $T_{\mathrm{s}} = 100\mathrm{ns}$ and the pulse bandwidth $B = 12.5\mathrm{GHz}$ are chosen. To assess the performance improvement of the ISAC receiver, we define λ as the incremental gain of N_{p}, which is given by

$$\lambda(N_{\mathrm{p}}) = \frac{P_{\mathrm{e,full}}(N_{\mathrm{p}})}{P_{\mathrm{e,full}}(N_{\mathrm{p,int}})}(\mathrm{or} \; \frac{\mathrm{CRLB}_{D,\mathrm{full}}(N_{\mathrm{p}})}{\mathrm{CRLB}_{D,\mathrm{full}}(N_{\mathrm{p,int}})}). \tag{22}$$

The prefixes "IG-BER" and "IG-CRLB" are used to represent the incremental gains $\lambda(N_{\mathrm{p}})$ of BER and CRLB respectively. We can notice that there is a dividing point $N_{\mathrm{p,div}} \approx 2N_{\mathrm{s}} = 5000$ differing two performance regions: $\lambda(N_{\mathrm{p}})$ of BER decreases rapidly in the region $(0, N_{\mathrm{p,div}}]$, while becomes almost flat in the region $(N_{\mathrm{p,div}}, +\infty)$. Unlike BER, $\lambda(N_{\mathrm{p}})$ of CRLB decreases with N_{p} and has no lower bound. Thus, in order to ensure the performance of the communication part, N_{p} should be kept within the region $(0, N_{\mathrm{p,div}}]$.

Another problem is how to choose an appropriate N_{p}. In practical applications, the ISAC system usually has the constraints on BER and MSE of the distance denoted as P and S respectively. To maximize data transmission resources, we can obtain minimum N_{p} satisfying both constraints. The result is given by

$$N_{\mathrm{p,min}} = \max\{P_{\mathrm{e,full}}^{-1}(P), \mathrm{MSE}_{\mathrm{full}}^{-1}(S)\}, \tag{23}$$

where $P_{\mathrm{e,full}}^{-1}(\cdot)$ is the inverse function of BER given in (12) about N_{p}, and $\mathrm{MSE}_{\mathrm{full}}^{-1}(\cdot)$ is the inverse function of MSE of the estimated distance about N_{p}. Because the relationship between the received signal and the distance is difficult to obtain, the relation between MSE and N_{p} can only be acquired from simulation.

IV. RECEIVER DESIGN WITH LOW RESOLUTION

The high time resolution of pulsed signals is beneficial to ranging. However, the large bandwidth of pulsed signal requires a high sampling rate. In practice, the cost of the full-resolution ADC with such a high sampling rate is excessive. Thus, the low-resolution ADC is attractive because of its lower hardware cost and lower power consumption compared with the full-resolution ADC.

In this section, the pulse-based ISAC receiver design with low-resolution ADC is discussed. We first propose a MLE method using PF to obtain CSI. Under the condition of the low-resolution quantization, we redesign the symbol detector based on minimum BER criterion for the data

recovery and the estimator based on NP rule for the ranging estimation. The BER and CRLB of the low-resolution ISAC receiver are also obtained in Section IV-C and Section IV-D. Finally, we discuss the key parameters in the low-resolution ISAC receiver design. The optimal quantization threshold vector is obtained in Section IV-E, and the analysis and allocation method of PF length are given in Section IV-F.

A. Low-resolution ADC

Assuming that the low-resolution ADC has the same quantization thresholds for positive and negative regions, the M-level ADC is given by

$$
x_{i,k} = \begin{cases}
l_1, & c_0 < r_{i,k} < c_1 \\
l_2, & c_1 \le r_{i,k} < c_2 \\
\ldots \\
l_{M-1}, & c_{M-2} \le r_{i,k} < c_{M-1} \\
l_M, & c_{M-1} \le r_{i,k} < c_M
\end{cases} \quad , \text{ for all } i,k \tag{24}
$$

where $\mathbf{c} = [c_0, c_1, ..., c_{[M/2]}]^T$ is a quantization threshold vector in negative regions with $c_0 < c_1 < ... < c_{[M/2]} \le 0$, $c_0 = -\infty$, and $\mathbf{l} = [l_1, ..., l_M]^T$ is the quantization level vector. Moreover, quantization thresholds in positive regions (including zero) are given by $c_m = -c_{M-m}$, $m = [M/2] + 1, ..., M$.

In the special case of $M = 2$, a monobit ADC is given by

$$
x_{i,k} = \begin{cases}
l_1, & -\infty \le r_{i,k} \le 0 \\
l_2, & 0 \le r_{i,k} \le +\infty
\end{cases} \quad , \text{ for all } i,k \tag{25}
$$

with $c_0 = -\infty$, $c_2 = +\infty$ and $c_1 = 0$. The monobit ADC only preserves the polarity of sample points and is equivalent to the sign detector.

Furthermore, we denote the output of the low-resolution ADC as the low-resolution sample point matrix $\mathbf{X} \in \mathbb{R}^{N_s \times N}$ whose entries are $x_{i,k}$. $\mathbf{X} = [\mathbf{X}_p, \mathbf{X}_d]$ is divided in the same way as $\mathbf{R}$, and their entries are denoted as $x_p^{(i,k_p)}$ and $x_d^{(i,k_d)}$. Then, $\mathbf{X}$ will be used in the following digital signal processing.

B. Channel Estimation

Similar to Section III-A, we first acquire CSI. The estimation of $\mathbf{w}$ is also obtained by the MLE method based on PF. Then, the log-likelihood function of $\mathbf{w}$ is given by

$$
L(\mathbf{X}_p | \mathbf{a}, \mathbf{w}) = \sum_{i=0}^{N_s-1} \sum_{m=1}^{M} N_i^m \cdot \log \Pr(x_p^{(i,k_p)} = l_m | w_i, a_{k_p}), \tag{26}
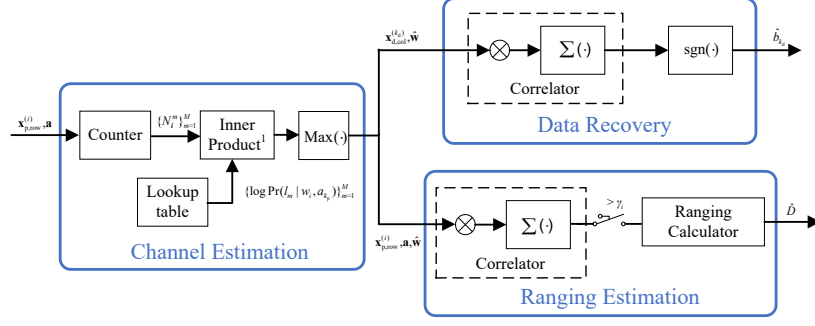$$

Fig. 4. The block diagram of the post quantization processing part of the low-resolution ISAC receiver

where N_i^m denotes the number of l_m at the ith sample points of PF, and $\Pr(x_{\mathrm{p}}^{(i,k_{\mathrm{p}})} = l_m|w_i, a_{k_{\mathrm{p}}})$ is the probability of $x_{\mathrm{p}}^{(i,k_{\mathrm{p}})} = l_m$ when w_i and $a_{k_{\mathrm{p}}}$ are known (i.e. $\Pr(\cdot|\cdot)$ is a conditional probability). From (26), we can decompose the estimation of $\mathbf{w}$ into its entries w_i.

$$L(\mathbf{x}_{\mathrm{p,row}}^{(i)}|\mathbf{a}, w_i) = \sum_{m=1}^{M} N_i^m \cdot \log \Pr(x_{\mathrm{p}}^{(i,k_{\mathrm{p}})} = l_m|w_i, a_{k_{\mathrm{p}}}),$$
$$i = 0, 1, \ \ldots \ , N_{\mathrm{s}} - 1 \tag{27}$$

where $\mathbf{x}_{\mathrm{p,row}}^{(i)}$ denotes the ith row vector of $\mathbf{X}_{\mathrm{p}}$. the MLE of w_i is given by

$$\hat{w}_i = \arg \max_{w_i} L(\mathbf{x}_{\mathrm{p,row}}^{(i)}|\mathbf{a}, w_i). \quad i = 0, 1, \ \ldots \ , N_{\mathrm{s}} - 1 \tag{28}$$

It is difficult to get a closed-form expression for the low-resolution ISAC receiver to estimate w_i. In practice, we use a lookup table. The table is indexed by w_i, and each row of the table stores M entries: $\{\log \Pr(l_m|w_i, a_{k_{\mathrm{p}}})\}_{m=1}^{M}$. For each N_i^m vector, we can perform the inner product of it with each row. The row which gives the maximum inner product corresponds to the MLE of w_i.

C. Data recovery

Unlike the full-resolution ISAC receiver, the low-resolution ISAC receiver recovers data symbols from $\mathbf{X}_{\mathrm{d}}$ whose entries are discrete random variables as

$$\mathrm{H}_1 : x_{\mathrm{d}}^{(i,k_{\mathrm{d}})} = l_m \sim f_m^{(i,k_{\mathrm{d}})}$$
$$\mathrm{H}_0 : x_{\mathrm{d}}^{(i,k_{\mathrm{d}})} = l_m \sim g_m^{(i,k_{\mathrm{d}})}, \tag{29}$$

---

[1]The inner product can be equivalent to matrix multiplication and the lookup table stores data in advance through read-only registers (ROM).

where $f_m^{(i,k_d)} = \Pr(x_d^{(i,k_d)} = l_m | r_d^{(i,k_d)} = w_i + n_d^{(i,k_d)})$, $g_m^{(i,k_d)} = \Pr(x_d^{(i,k_d)} = l_m | r_d^{(i,k_d)} = -w_i + n_d^{(i,k_d)})$. With $p(H_0) = p(H_1) = \frac{1}{2}$, the LLRT of the k_dth symbol based on minimum BER criterion is given by

$$\Lambda_d(\mathbf{x}_{d,\text{col}}^{(k_d)}) = \sum_{i=0}^{N_s-1} \log \frac{f_m^{(i,k_d)}}{g_m^{(i,k_d)}} \underset{H_0}{\overset{H_1}{\gtrless}} 0, \tag{30}$$

where $\mathbf{x}_{d,\text{col}}^{(k_d)}$ denotes the k_dth column vector of $\mathbf{X}_d$. It is too complicated to use LLRT for data recovery because of the non-linear calculation of $\log(\cdot)$.

To simplify (30), we use the linear symbol detector which can be obtained from the Taylor series expansion of (30) at $\mathbf{w} = 0$. Define $F_n(\cdot)$ as the CDF of $f_n(\cdot)$, and let $r_d^{(i,k_d)}$ be in the quantization interval $[c_{m_{i,k_d}-1}, c_{m_{i,k_d}}]$ (i.e. $x_d^{(i,k_d)} = l_{m_{i,k_d}}$). Then, we have $f_m^{(i,k_d)} = F_n(c_{m_{i,k_d}} - w_i) - F_n(c_{m_{i,k_d}-1} - w_i)$, $g_m^{(i,k_d)} = F_n(c_{m_{i,k_d}} + w_i) - F_n(c_{m_{i,k_d}-1} + w_i)$. A linear approximation of (30) is obtained by the approximate formula $F_n(c_{m_{i,k_d}} \pm w_i) = F_n(c_{m_{i,k_d}}) \pm w_i f_n(c_{m_{i,k_d}})$ and Taylor series expansion $\log \frac{f_m^{(i,k_d)}}{g_m^{(i,k_d)}} \approx \frac{f_m^{(i,k_d)}}{g_m^{(i,k_d)}} - 1$. That is,

$$\begin{aligned}
\Lambda_d(\mathbf{x}_{d,\text{col}}^{(k_d)}) &= \sum_{i=0}^{N_s-1} \log \frac{f_m^{(i,k_d)}}{g_m^{(i,k_d)}} \\
&\approx \sum_{i=0}^{N_s-1} \left(\frac{F_n(c_{m_{i,k_d}} - w_i) - F_n(c_{m_{i,k_d}-1} - w_i)}{F_n(c_{m_{i,k_d}} + w_i) - F_n(c_{m_{i,k_d}-1} + w_i)} - 1 \right) \\
&\approx \sum_{i=0}^{N_s-1} 2w_i \frac{f_n(c_{m_{i,k_d}-1}) - f_n(c_{m_{i,k_d}})}{F_n(c_{m_{i,k_d}}) - F_n(c_{m_{i,k_d}-1})}.
\end{aligned} \tag{31}$$

The linear symbol detector can be written as

$$C_{\text{low}}(\mathbf{x}_{d,\text{col}}^{(k_d)}, \mathbf{w}) = \sum_{i=0}^{N_s-1} w_i \frac{f_n(c_{m_{i,k_d}-1}) - f_n(c_{m_{i,k_d}})}{F_n(c_{m_{i,k_d}}) - F_n(c_{m_{i,k_d}-1})} \underset{H_0}{\overset{H_1}{\gtrless}} 0. \tag{32}$$

The communication part of the post quantization processing shown in Fig. 4 is designed according to (28) and (32). The quantization level in (24) can be set to

$$x_{i,k} = l_m = \frac{f_n(c_{m-1}) - f_n(c_m)}{F_n(c_m) - F_n(c_{m-1})}. \quad r_{i,k} \in [c_{m-1}, c_m) \tag{33}$$

Note that the values of quantization levels are constant and only dependent on the quantization threshold vector $\mathbf{c}$. The channel estimation uses a lookup table method, as mentioned in Section IV-B. The test statistic (32) can be directly obtained by the inner product of $\hat{\mathbf{w}}$ and $\mathbf{x}_{d,\text{col}}^{(k_d)}$, which is given by

$$\begin{aligned}
\langle \hat{\mathbf{w}}, \mathbf{x}_{d,\text{col}}^{(k_d)} \rangle &= \sum_{i=0}^{N_s-1} \hat{w}_i x_d^{(i,k_d)} \\
&= \sum_{i=0}^{N_s-1} \hat{w}_i \frac{f_n(c_{m_{i,k_d}}) - f_n(c_{m_{i,k_d}})}{F_n(c_{m_{i,k_d}}) - F_n(c_{m_{i,k_d}})}.
\end{aligned} \tag{34}$$

Finally, the data symbols are given by the output of the sign detector.

We analyze the BER of the detector (32). At first, when $N_{\text{p}} \gg 1$, we can approximate the channel estimation error $\tilde{\mathbf{w}}$ as a Gaussian random variable vector, which is based on Lemma 1.

Lemma 1 (The asymptotic distribution of $\hat{\mathbf{w}}$). *Under the condition of large data records ($N_{\text{p}} \gg 1$), the MLE of $\mathbf{w}$ can be asymptotically distributed according to*

$$\hat{\mathbf{w}} \sim \mathcal{CN}(\mathbf{w}, \boldsymbol{F}_{\mathbf{w}}^{-1}), \tag{35}$$

where the autocorrelation matrix $\boldsymbol{F}_{\mathbf{w}}^{-1}$ is given by

$$\boldsymbol{F}_{\mathbf{w}}^{-1} = \frac{\sigma_{\text{n}}^2}{N_{\text{p}}} \cdot \text{diag}\{\alpha_{w_0}^{-1}, \alpha_{w_1}^{-1}, \ \cdots \ , \alpha_{w_{N_{\text{s}}-1}}^{-1}\}, \tag{36}$$

where

$$\alpha_{w_i} = \sum_{m=1}^{M} \frac{\left(\phi\left(\frac{c_m - w_i}{\sigma_{\text{n}}}\right) - \phi\left(\frac{c_{m-1} - w_i}{\sigma_{\text{n}}}\right) \right)^2}{\Phi\left(\frac{c_m - w_i}{\sigma_{\text{n}}}\right) - \Phi\left(\frac{c_{m-1} - w_i}{\sigma_{\text{n}}}\right)} \tag{37}$$

is the quantization efficiency of the ith sample point, with $\phi(\cdot)$ being the PDF of the standard normal distribution.

Proof. The proof is given in Appendix C. $\qquad\square$

Subsequently, the BER of the detector (32) considering the channel estimation error is in Proposition 3.

Proposition 3 (BER of the low-resolution symbol detector). *Considering the channel estimation error and under the condition of large sample points ($N_{\text{s}} \gg 1, N_{\text{p}} \gg 1$), the BER of $C_{\text{low}}(\mathbf{x}_{\text{d,col}}^{(k_{\text{d}})}, \hat{\mathbf{w}})$ is given by*

$$P_{\text{e,low}} = Q\left(\sqrt{\frac{2\alpha_0 \cdot \mu\text{SNR}}{1 + \frac{N_{\text{s}}}{N_{\text{p}}}(2\alpha_0 \cdot \mu\text{SNR})^{-1}}} \right), \tag{38}$$

where

$$\alpha_0 = \sum_{m=1}^{M} \frac{\left(\phi\left(\frac{c_m}{\sigma_{\text{n}}}\right) - \phi\left(\frac{c_{m-1}}{\sigma_{\text{n}}}\right) \right)^2}{\Phi\left(\frac{c_m}{\sigma_{\text{n}}}\right) - \Phi\left(\frac{c_{m-1}}{\sigma_{\text{n}}}\right)} \tag{39}$$

is the quantization efficiency of the signal strength $w_i = 0$.

Proof. The proof is given in Appendix D. $\qquad\square$

Remark 2 (The effect of the quantization efficiency α_0). *Compared with (12), (38) involves the effect of the low-resolution quantization. The quantization efficiency α_0 is used to describe the performance loss caused by the low-resolution quantization, and $\alpha_0 \in [0, 1]$. We can provide a*

simple proof in the following. It can be seen that when $M \to +\infty$, the full-resolution quantization can be achieved, and α_0 reaches the maximum value. That is,

$$
\begin{aligned}
\lim_{M \to +\infty} \alpha_0 &= \lim_{M \to +\infty} \sum_{m=1}^{M} \frac{\left(\phi'(\frac{c_{m-1}}{\sigma_n}) \right)^2}{\Phi'(\frac{c_{m-1}}{\sigma_n})} (c_m - c_{m-1}) \\
&= \lim_{M \to +\infty} \sum_{m=1}^{M} \left(\frac{c_{m-1}}{\sigma_n} \right)^2 \phi(\frac{c_{m-1}}{\sigma_n})(\frac{c_m}{\sigma_n} - \frac{c_{m-1}}{\sigma_n}) \\
&= \frac{1}{\sqrt{2\pi}} \int_{-\infty}^{+\infty} x^2 e^{-\frac{x^2}{2}} dx \\
&= 1.
\end{aligned}
\tag{40}
$$

Because $\lim_{M \to +\infty} c_m - c_{m-1} = 0$, $m = 1, 2, ..., M$, we have the Taylor series expansion $\phi(\frac{c_m}{\sigma_n}) - \phi(\frac{c_{m-1}}{\sigma_n}) = \phi'(\frac{c_{m-1}}{\sigma_n})(c_m - c_{m-1})$, $\Phi(\frac{c_m}{\sigma_n}) - \Phi(\frac{c_{m-1}}{\sigma_n}) = \Phi'(\frac{c_{m-1}}{\sigma_n})(c_m - c_{m-1})$ substituted in the first step of (40). We notice that when $M \to +\infty$, $\alpha_0 = 1$, the low-resolution symbol detector (32) will be converted to the full-resolution symbol detector (11), and BER will yield to (12).

D. Ranging Estimation

Using $\mathbf{X}_p$, we can employ the threshold detection method for ranging. At first, the detection of the signal arrival can be modeled as

$$
\begin{aligned}
H_1 &: x_p^{(i,k_p)} = l_m \sim p_m^{(i,k_p)} \\
H_0 &: x_p^{(i,k_p)} = l_m \sim q_m^{(i,k_p)},
\end{aligned}
\tag{41}
$$

where $p_m^{(i,k_p)} = \Pr(x_p^{(i,k_p)} = l_m | r_p^{(i,k_p)} = a_{k_p} w_i + n_p^{(i,k_p)})$, $q_m^{(i,k_p)} = \Pr(x_p^{(i,k_p)} = l_m | r_p^{(i,k_p)} = n_p^{(i,k_p)})$. The LLR of the ith sample point is given by

$$
\Lambda_r(\mathbf{x}_{p,row}^{(i)}) = \sum_{k=0}^{N_p - 1} \log \frac{p_m^{(i,k_p)}}{q_m^{(i,k_p)}},
\tag{42}
$$

where $\mathbf{x}_{p,row}^{(i)}$ denotes the ith row vector of $\mathbf{X}_p$. Let $r_p^{(i,k_p)}$ be in the quantization interval $[c_{\overline{m}_{i,k_p}-1}, c_{\overline{m}_{i,k_p}}]$ (i.e. $x_p^{(i,k_p)} = l_{\overline{m}_{i,k_p}}$). Note that $p_m^{(i,k_p)} = F_n(c_{\overline{m}_{i,k_p}} - a_{k_p} w_i) - F_n(c_{\overline{m}_{i,k_p}-1} - a_{k_p} w_i)$ and $q_m^{(i,k_p)} = F_n(c_{\overline{m}_{i,k_p}}) - F_n(c_{\overline{m}_{i,k_p}-1})$. To avoid the non-linear calculation of $\log(\cdot)$, a linear

approximation of (42) can be obtained by using the approximate formula $F_{\mathrm{n}}(c_{\overline{m}_{i,k_{\mathrm{p}}}} \pm w_i) \approx$ $F_{\mathrm{n}}(c_{\overline{m}_{i,k_{\mathrm{p}}}}) \pm w_i f_{\mathrm{n}}(c_{\overline{m}_{i,k_{\mathrm{p}}}})$ and the Taylor series expansion $\log \frac{p_m^{(i,k_{\mathrm{p}})}}{q_m^{(i,k_{\mathrm{p}})}} \approx \frac{p_m^{(i,k_{\mathrm{p}})}}{q_m^{(i,k_{\mathrm{p}})}} - 1$.

$$
\begin{aligned}
\Lambda_{\mathrm{r}}(\mathbf{x}_{\mathrm{p,row}}^{(i)}) &= \sum_{k=0}^{N_{\mathrm{p}}-1} \log \frac{p_m^{(i,k_{\mathrm{p}})}}{q_m^{(i,k_{\mathrm{p}})}} \\
&\approx \sum_{k=0}^{N_{\mathrm{p}}-1} \left(\frac{f_{\mathrm{n}}(c_{\overline{m}_{i,k_{\mathrm{p}}}} - a_{k_{\mathrm{p}}} w_i) - f_{\mathrm{n}}(c_{\overline{m}_{i,k_{\mathrm{p}}}-1} - a_{k_{\mathrm{p}}} w_i)}{F_{\mathrm{n}}(c_{\overline{m}_{i,k_{\mathrm{p}}}}) - F_{\mathrm{n}}(c_{\overline{m}_{i,k_{\mathrm{p}}}-1})} - 1 \right) \\
&\approx w_i \sum_{k=0}^{N_{\mathrm{p}}-1} a_{k_{\mathrm{p}}} \frac{f_{\mathrm{n}}(c_{\overline{m}_{i,k_{\mathrm{p}}}-1}) - f_{\mathrm{n}}(c_{\overline{m}_{i,k_{\mathrm{p}}}})}{F_{\mathrm{n}}(c_{\overline{m}_{i,k_{\mathrm{p}}}}) - F_{\mathrm{n}}(c_{\overline{m}_{i,k_{\mathrm{p}}}-1})}.
\end{aligned}
\tag{43}
$$

By eliminating the amplitude of w_i, the linear signal detector can be given by

$$
R_{\mathrm{low}}(\mathbf{x}_{\mathrm{p,row}}^{(i)}, \mathbf{a}, w_i) = \mathrm{sgn}(w_i) \cdot \sum_{k=0}^{N_{\mathrm{p}}-1} a_{k_{\mathrm{p}}} \frac{f_{\mathrm{n}}(c_{\overline{m}_{i,k_{\mathrm{p}}}-1}) - f_{\mathrm{n}}(c_{\overline{m}_{i,k_{\mathrm{p}}}})}{F_{\mathrm{n}}(c_{\overline{m}_{i,k_{\mathrm{p}}}}) - F_{\mathrm{n}}(c_{\overline{m}_{i,k_{\mathrm{p}}}-1})} \underset{\mathrm{H_0}}{\overset{\mathrm{H_1}}{\gtrless}} \gamma_i.
\tag{44}
$$

When N_{p} is large enough, $R_{\mathrm{low}}(\mathbf{x}_{\mathrm{p,row}}^{(i)}, \mathbf{a}, w_i)$ can be approximated as a Gaussian random variable by using the central limit theorem. Thus, the threshold based on NP rule with a constant false alarm rate ϵ can be set to

$$
\gamma_i = \Phi^{-1}(1 - \epsilon) \sqrt{\mathrm{var}[R_{\mathrm{low}}(\mathbf{x}_{\mathrm{p,row}}^{(i)}, \mathbf{a}, w_i)|\mathrm{H_0}]} + \mathrm{E}[R_{\mathrm{low}}(\mathbf{x}_{\mathrm{p,row}}^{(i)}, \mathbf{a}, w_i)|\mathrm{H_0}].
\tag{45}
$$

Finally, ToA is calculated as

$$
\tau_1 = T_{\mathrm{sam}} \min_i \{i | R_{\mathrm{low}}(\mathbf{x}_{\mathrm{p,row}}^{(i)}, \mathbf{a}, w_i) > \gamma_i\} - T_{\mathrm{sam}}/2.
\tag{46}
$$

The ranging part of the post quantization processing shown in Fig. 4 is designed according to (28) and (44). By reusing the result of channel estimation module, the ranging estimation module calculates the inner product of $\mathrm{sgn}(\hat{w}_i) \cdot \mathbf{a}$ and $\mathbf{x}_{\mathrm{p,row}}^{(i)}$ by utilizing a correlator, and then performs the threshold detection to estimate ToA. The distance measurement can be acquired from the ToA of the returned packet.

The CRLB of the low-resolution ISAC receiver is analyzed in Proposition 4.

Proposition 4 (CRLB of D with low resolution). *Considering a linear relationship that* $\mathrm{CRLB}_{D,\mathrm{low}} = c^2 \cdot \mathrm{CRLB}_{\tau_1,\mathrm{low}}$ *and the effect of the low-resolution quantization on the ranging estimation, we can evaluate the CRLB of D as*

$$
\mathrm{CRLB}_{D,\mathrm{low}} = \frac{c^2}{8\pi^2(1-\eta)N_{\mathrm{p}}\beta^2\alpha_0\mu\mathrm{SNR}_{\mathrm{p}}}.
\tag{47}
$$

Proof. The proof is given in Appendix E. $\square$

TABLE II

OPTIMAL QUANTIZATION THRESHOLD VECTOR OF M-LEVEL ADC

M-level	Quantization Threshold Vector
2	$\{-\infty, 0, +\infty\}$
3	$\{-\infty, -0.610\sigma_\mathrm{n}, 0.610\sigma_\mathrm{n}, +\infty\}$
4	$\{-\infty, -0.982\sigma_\mathrm{n}, 0, 0.982\sigma_\mathrm{n}, +\infty\}$

E. Quantization Threshold Vector Design

When pulsed signals are input to the low-resolution ADC, the lower quantization thresholds will cause the signal to be clipped, while the higher quantization thresholds will make the resolution of signal too low. Thus, the optimal quantization threshold vector $\mathbf{c}_\mathrm{opt}$ should be chosen. In the above sections, we use $P_\mathrm{e,low}$ and $\mathrm{CRLB}_{D,\mathrm{low}}$ as the performance metrics of the low-resolution ISAC receiver. As mentioned in Proposition 3 and Proposition 4, both BER and CRLB of the low-resolution quantization decrease when α_0 increases. Thus, we can obtain $\mathbf{c}_\mathrm{opt}$ by maximizing α_0. When M is even, we have

$$
\begin{aligned}
\mathbf{c}_\mathrm{opt} &= \arg\max_{\mathbf{c}} \alpha_0 \\
&= \arg\max_{\mathbf{c}} \sum_{m=1}^{[M/2]} 2\frac{\left(\phi(\frac{c_m}{\sigma_\mathrm{n}}) - \phi(\frac{c_{m-1}}{\sigma_\mathrm{n}})\right)^2}{\Phi(\frac{c_m}{\sigma_\mathrm{n}}) - \Phi(\frac{c_{m-1}}{\sigma_\mathrm{n}})},
\end{aligned}
\tag{48}
$$

or when M is odd, we have

$$
\begin{aligned}
\mathbf{c}_\mathrm{opt} &= \arg\max_{\mathbf{c}} \alpha_0 \\
&= \arg\max_{\mathbf{c}} \left\{ \sum_{m=1}^{[M/2]} 2\frac{\left(\phi(\frac{c_m}{\sigma_\mathrm{n}}) - \phi(\frac{c_{m-1}}{\sigma_\mathrm{n}})\right)^2}{\Phi(\frac{c_m}{\sigma_\mathrm{n}}) - \Phi(\frac{c_{m-1}}{\sigma_\mathrm{n}})} + \frac{\left(\phi(\frac{c_{[M/2]+1}}{\sigma_\mathrm{n}}) - \phi(\frac{c_{[M/2]}}{\sigma_\mathrm{n}})\right)^2}{\Phi(\frac{c_{[M/2]+1}}{\sigma_\mathrm{n}}) - \Phi(\frac{c_{[M/2]}}{\sigma_\mathrm{n}})} \right\}.
\end{aligned}
\tag{49}
$$

By letting $\frac{\partial \alpha_0}{\partial c_m} = 0$, $m = 1, 2, ..., [M/2]$, $\mathbf{c}_\mathrm{opt}$ is calculated as

$$
\begin{aligned}
\frac{c_{m,\mathrm{opt}}}{\sigma_\mathrm{n}} &= \frac{1}{2}\left(\frac{\phi(\frac{c_{m-1,\mathrm{opt}}}{\sigma_\mathrm{n}}) - \phi(\frac{c_{m,\mathrm{opt}}}{\sigma_\mathrm{n}})}{\Phi(\frac{c_{m,\mathrm{opt}}}{\sigma_\mathrm{n}}) - \Phi(\frac{c_{m-1,\mathrm{opt}}}{\sigma_\mathrm{n}})} + \frac{\phi(\frac{c_{m,\mathrm{opt}}}{\sigma_\mathrm{n}}) - \phi(\frac{c_{m+1,\mathrm{opt}}}{\sigma_\mathrm{n}})}{\Phi(\frac{c_{m+1,\mathrm{opt}}}{\sigma_\mathrm{n}}) - \Phi(\frac{c_{m,\mathrm{opt}}}{\sigma_\mathrm{n}})} \right), \\
&\qquad\qquad m = 1, 2, \ldots, [M/2]
\end{aligned}
\tag{50}
$$

whether M is odd or even. We can get the optimal quantization threshold vectors of low-resolution ISAC receivers (i.e. 2-4 level) through using a fixed-point iteration method [57] once the initial thresholds are decided as

$$c_0 = -\infty,$$

$$c_{[M/2]} = \begin{cases} 0 & M \text{ is even} \\ -c_{[M/2]+1} & M \text{ is odd} \end{cases}. \tag{51}$$

Note that the convergence of the fixed-point iteration method is proved by Banach fixed point theorem [57]. Finally, the optimal quantization threshold vectors of $M = 2, 3, 4$ are given in Table. II.

F. PF Length Design

In the low-resolution ISAC receiver, the effect of PF length N_{p} is also discussed. We use the incremental gain $\lambda(N_{\mathrm{p}})$ to assess the performance improvement brought by the increase of N_{p}, which is given by

$$\lambda(N_{\mathrm{p}}) = \frac{P_{\mathrm{e,low}}(N_{\mathrm{p}})}{P_{\mathrm{e,low}}(N_{\mathrm{p,int}})} (\text{or } \frac{\mathrm{CRLB}_{D,\mathrm{low}}(N_{\mathrm{p}})}{\mathrm{CRLB}_{D,\mathrm{low}}(N_{\mathrm{p,int}})}). \tag{52}$$

In Fig. 5(a), we provide $\lambda(N_{\mathrm{p}})$ of BER and CRLB at various N_{p} and SNR. In this figure, we choose $N_{\mathrm{p,int}} = 600$, $T_{\mathrm{s}} = 100\mathrm{ns}$ and $B = 12.5\mathrm{GHz}$, and the optimal quantization threshold vector $\mathbf{c}^{\mathrm{opt}}$ mentioned in Section IV-E is used. It is shown that the number of quantization levels M only affects the declining rate of $\lambda(N_{\mathrm{p}})$ of BER in small N_{p} case, while is irrelevant to the dividing point $N_{\mathrm{p,div}}$. In the end, we come to the same conclusion as the full-resolution ISAC receiver described in Section III-D.

For the low-resolution ISAC receiver with the constraints of BER P and MSE S, the PF length design based on maximum data transmission capability criterion is given by

$$N_{\mathrm{p,min}} = \max\{P_{\mathrm{e,low}}^{-1}(P), \mathrm{MSE}_{\mathrm{low}}^{-1}(S)\}, \tag{53}$$

where $P_{\mathrm{e,low}}^{-1}(\cdot)$ is the inverse function of the BER of the low-resolution symbol detector (38) about N_{p}, and $\mathrm{MSE}_{\mathrm{low}}^{-1}(\cdot)$ is the inverse function of the MSE of the distance estimated by the low-resolution ISAC receiver about N_{p}.

V. SIMULATION RESULTS AND DISCUSSION

In this section, we provide the simulation results for the proposed ISAC receiver. We employ the standard CM1 channel model for simulation with 1000 realizations [58], and the impulse
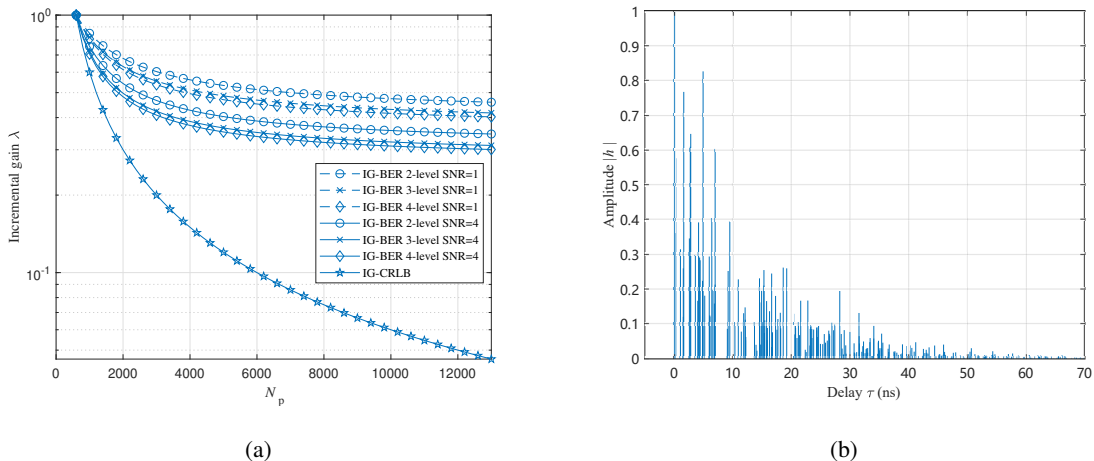
Fig. 5. (a) Analytical $\lambda(N_\mathrm{p})$ of the low-resolution ISAC receiver at various N_p and SNRs, (b) The impulse response of the standard CM1 channel with the normalized amplitude $|h|$

response of the standard CM1 channel in one realization is given in Fig. 5(b). The transmitted pulse is chosen to be a second order derivative Gaussian pulse

$$p(t) = \left[1 - \left(\frac{t}{\tau_\mathrm{ps}}\right)^2\right] \cdot \exp\left[-2\pi \left(\frac{t}{\tau_\mathrm{ps}}\right)^2\right], \tag{54}$$

where $\tau_\mathrm{ps} = 0.29\mathrm{ns}$ is a time constant which controls the pulse duration (i.e. about 0.7 ns) [59]. The ToA of the received signal is uniformly distributed over [0ns, 50ns]. The symbol duration T_s is 100ns. Then, the impulse response of LPF is given by

$$h_\mathrm{LPF}(t) = \frac{\sin(2\pi Bt)}{\pi t}, \tag{55}$$

where the filter bandwidth B is 12.5GHz. The sampling interval T_sam is 40ps. The optimal quantization thresholds of the low-resolution ADC mentioned in Section IV-E are used. For the channel estimation of the low-resolution ISAC receiver, we use a lookup table quantizing s_i in [-5,5] with a step size 0.005. The false alarm probability ϵ is appropriately set to 10^{-7}. All parameters conform to the standard IEEE 802.15.4z [60], and are summarized at Table III.

In Fig. 6(a) and Fig. 6(b), we compare the performance of the proposed ISAC system (denoted as "MLE") with full-resolution (denoted as "FR") and M-level quantization, the GML-based receiver at $N_\mathrm{p} = 1000$ [42] and the TRPC-based receiver at $N_\mathrm{d} = 1000$ [41], [43]. The computational complexity and signaling overhead of these ISAC receivers are shown in Table IV. Note that N_T and N_G are the iteration times of the TRPC-based receiver and the GML-based receiver and N_L is the number of quantization levels of the lookup table. It is shown
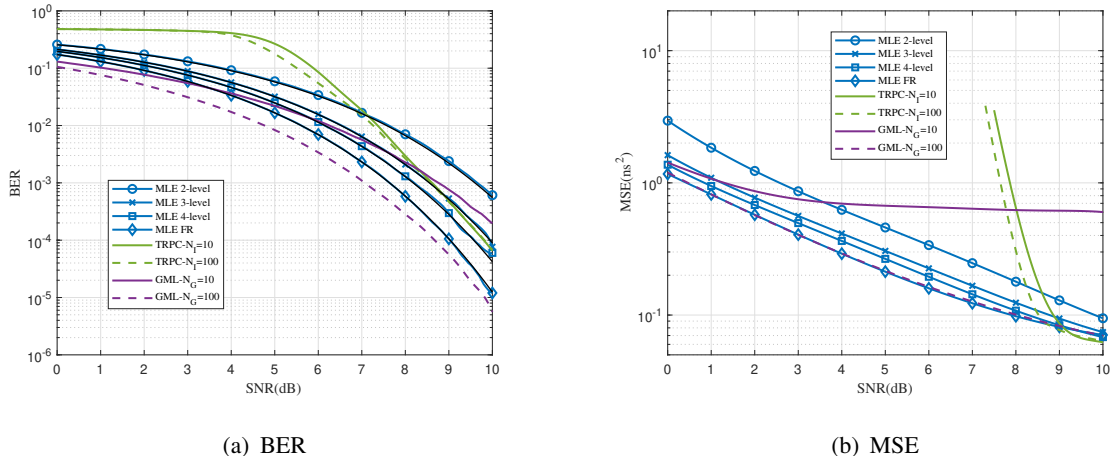
(a) BER

(b) MSE

Fig. 6. BER and MSE performance of the full-resolution and M-level ($M = 2, 3, 4$) MLE-based receivers, the TRPC-based receiver and the GML-based receiver at various SNRs and $N_\mathrm{p} = 1000$ (the simulation results of the MLE-based receivers denoted as blue lines and the theoretical results denoted as black lines)

TABLE III

PARAMETERS FOR SIMULATION ANALYSIS

		Parameter value
Shaping pulse (54)	Pulse parameter τ_ps	0.29 ns
Packet structure (1)	Symbol duration T_s	100 ns
	PF length N_p	500 - 3000
	DF length N_d	5000
M-level ADC (II)	Sampling interval T_sam	40ps
	Quantization precision M	2 - 4 level
Low-pass filter (55)	Passband width B	12.5 GHz
Lookup table	Searching range	[-5 , 5]
	Searching step	0.005
NP rule(17),(45)	False alarm probability	10^{-7}

that for full resolution, the TRPC-based receiver has an advantage of extremely low signaling overhead by reusing DF for the channel estimation iteratively. The GML-based receiver obtains CSI by many times of iterative calculations, and the computational complexity of one iterative calculation is mainly dependent on the estimation of delay which occupies the main computation overhead. Only one delay estimation requires $\mathrm{O}(N_\mathrm{s}^2)$ (i.e. about $10^6 \sim 10^8$ in this simulation, $N_\mathrm{s} \in [10^3, 10^4]$) additions and multiplications. The proposed full-resolution MLE method can achieve CSI with low cost because of adopting the closed-form solution, while for low resolution, the MLE method is realized by using the lookup table to search CSI. The computational
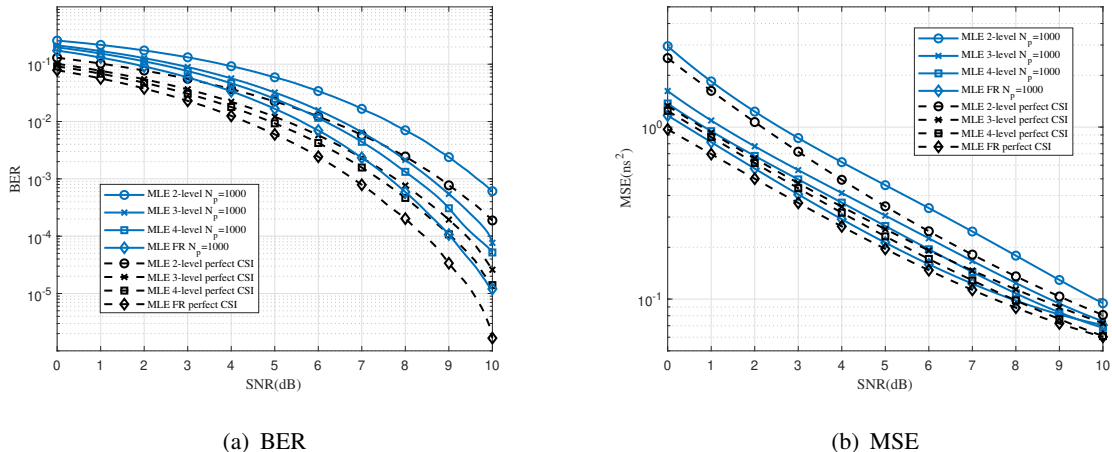
(a) BER

(b) MSE

Fig. 7. BER and MSE performance of the pulsed-based ISAC receiver with perfect CSI and estimated CSI at $N_{\mathrm{p}} = 1000$
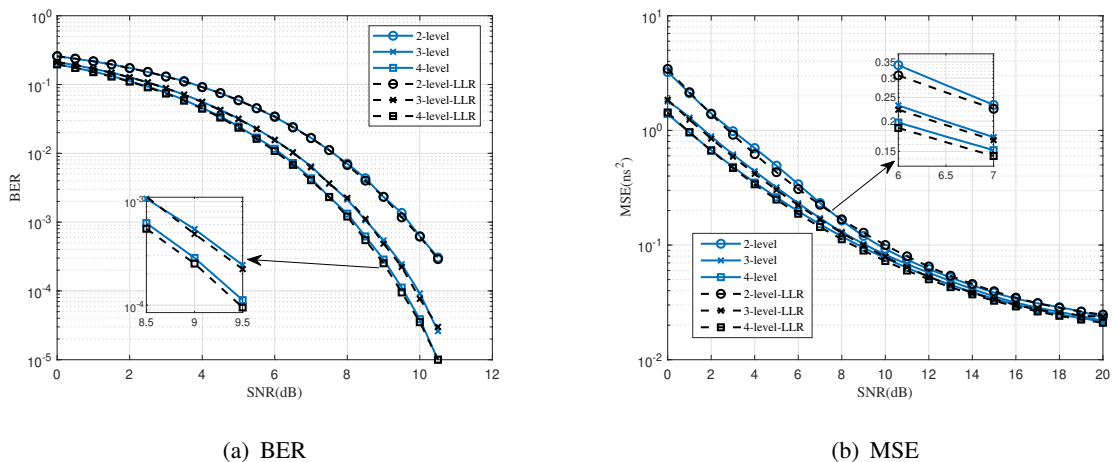

(a) BER

(b) MSE

Fig. 8. BER and MSE performance of the pulsed-based ISAC receiver with LLR and its linear approximation at $N_{\mathrm{p}} = 1000$

complexity of the lookup table method depends on the estimated range and step, which can be adjusted to meet requirements. From simulation, it can be seen that the GML-based receiver with $N_{\mathrm{G}} = 100$ has the best performance. The TRPC-based receiver makes a good performance in a high SNR case, but its performance is very bad at low SNR, because of the inaccurate channel estimation caused by high BER. The proposed full-resolution MLE receiver has about 1dB SNR loss in BER and near the same ranging accuracy compared with the GML-based receiver with $N_{\mathrm{G}} = 100$. The performance gap between the full-resolution ISAC receivers with perfect CSI and estimated CSI is shown in Fig. 7(a) and Fig. 7(b). Compared with the receiver with perfect CSI, the MLE receiver with $N_{\mathrm{p}} = 1000$ has about 1.5dB SNR loss in BER and
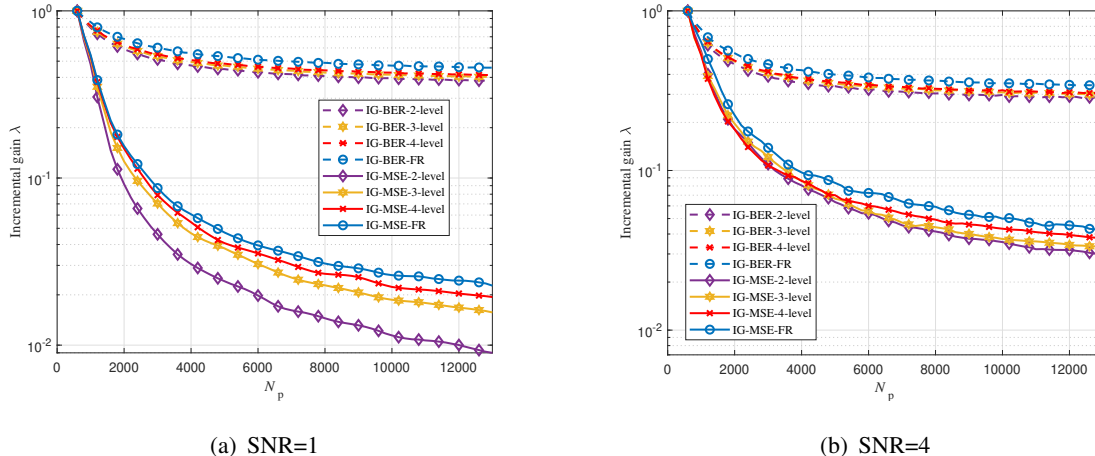
(a) SNR=1   (b) SNR=4

Fig. 9. $\lambda(N_\mathrm{p})$ of the full-resolution and M-level ISAC receivers ($M = 2, 3, 4$) at various N_p and SNRs

TABLE IV

COMPUTATIONAL COMPLEXITY AND SIGNALING OVERHEAD OF ISAC RECEIVERS

| | M-level | Full Resolution | | |
	MLE	TRPC	GML	MLE
Addition	$\mathrm{O}(MN_\mathrm{L}N_\mathrm{s})$	$\mathrm{O}(N_\mathrm{T}N_\mathrm{d}N_\mathrm{s})$	$\mathrm{O}(N_\mathrm{G}N_\mathrm{s}^2)$	$\mathrm{O}(N_\mathrm{p}N_\mathrm{s})$
Multiplication	$\mathrm{O}(MN_\mathrm{L}N_\mathrm{s})$	None	$\mathrm{O}(N_\mathrm{G}N_\mathrm{s}^2)$	None
PF Overhead	N_p	1	N_p	N_p

0.4dB SNR loss in MSE. Also, in Fig. 6(a), the theoretical results from (12) and (38) denoted as black lines are almost equal to the simulation results denoted as blue lines.

Then, we discuss the performance of the proposed ISAC receiver with different quantizations. In Fig. 6(a) and Fig. 6(b), it is shown that the full-resolution receiver has the best performance in both data recovery and ranging estimation, and the performance of the low-resolution receiver improves with the increase of M. For example, the 3-level ISAC receiver has a gain of 1dB in SNR for BER and of 1.2dB in SNR for MSE over the 2-level ISAC receiver, and about 0.4dB SNR loss for both BER and MSE compared with the 4-level ISAC receiver. Also, compared with the full-resolution ISAC receiver, the SNR gaps of the 3-level ISAC receiver in BER and MSE are around 0.8dB and 1dB respectively. It is noticed that the gain from using an additional quantization level decreases and 3-level quantization can obtain near the full-resolution performance (about 1dB SNR gap) with low ADC cost. With further increasing the number of quantization levels, the ISAC receiver can only achieve a limited performance gain (within 1dB) but lead to the rapidly increasing ADC cost. Thus, the 3-level receiver can be an attractive
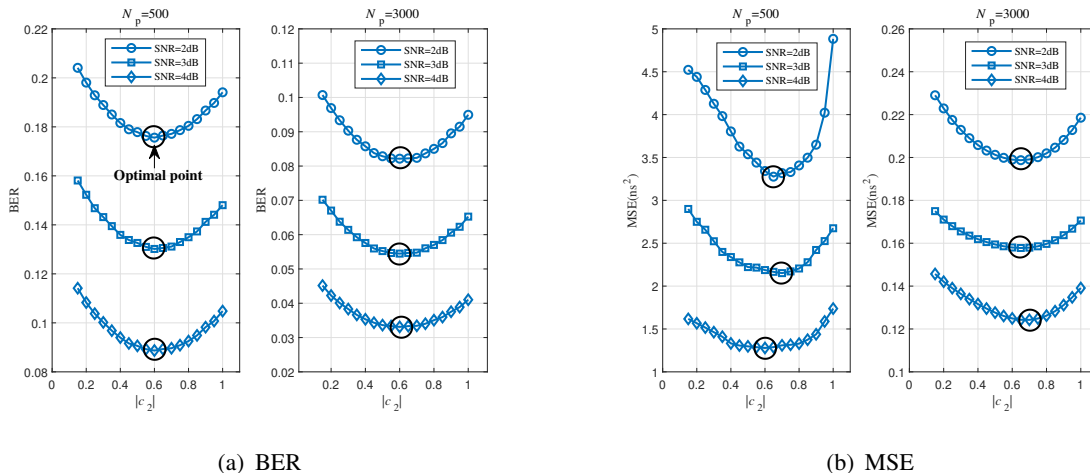
(a) BER

(b) MSE

Fig. 10. BER and MSE performance of the 3-level ISAC receiver at various quantization thresholds $|c_2|$
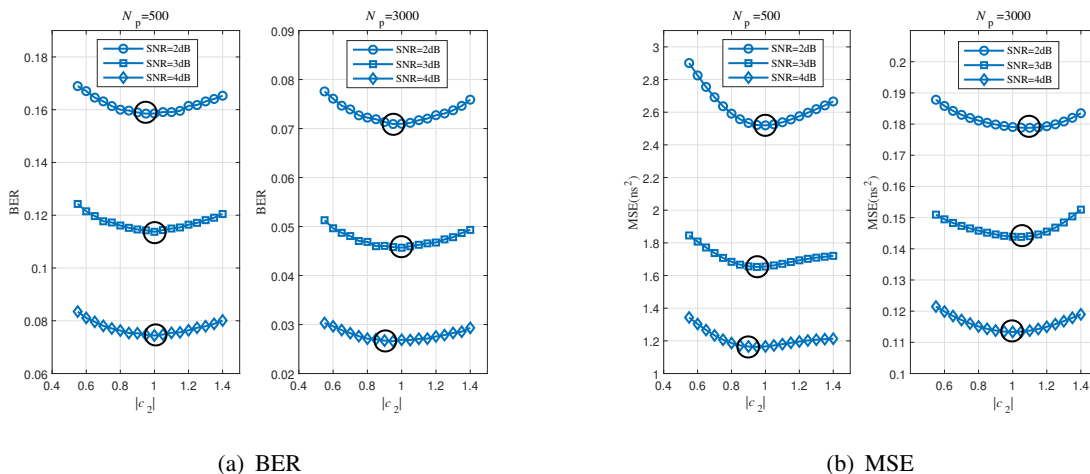

(a) BER

(b) MSE

Fig. 11. BER and MSE performance of the 4-level ISAC receiver at various quantization thresholds $|c_2|$

solution to make the tradeoff between the cost and the performance.

In Fig. 8(a) and Fig. 8(b), we discuss the performance loss caused by an inaccurate linear approximation of LLR. The postfix "LLR" represents the pulse-based ISAC receiver using LLR instead of its linear approximation. The simulation results prove that the performance loss caused by the inaccurate linear approximation is small enough to be ignored when SNR< 11dB. Although the performance loss will continuously increase with SNR, we think this loss is unimportant in a high SNR region (SNR> 11dB) because the receivers with the linear approximation of LLR have a sufficiently good performance for ISAC applications (BER$< 10^{-3}$,MSE< 0.1ns^2,when SNR> 11dB). Thus, a linear approximation of LLR can be used as a perfect substitute for

avoiding the infeasible non-linear calculation $\log(\cdot)$.

In Fig. 9(a) and Fig. 9(b), the effect of N_p is investigated. It shows that MSE performance is sensitive to the change of N_p, while BER is not when N_p is large (i.e. $N_p > 2N_s = 5000$). This agrees with the observations in Section III-D and Section IV-F. But unlike the theoretical performance of the ideal ranging estimation, it is noted that the accuracy of the ranging estimation has a lower bound in the practical applications because the threshold detection method has an inevitable gap with the real ToA deriving from the discretization processing. As a result, when SNR or M increases, MSE will decrease but the declining rate of $\lambda(N_p)$ of MSE reduces. In this paper, we mainly consider the pulse-based ISAC system working in a low SNR case, and hence the error caused by the discretization processing is not considered as a primary factor of the ranging estimation.

The optimal quantization threshold vector mentioned in Section IV-E is also proved to be valid by simulation. We provide BER and CRLB of the 3-level ISAC receiver at various quantization thresholds $|c_2|$ in a low SNR and different PF length case in Fig. 10(a) and Fig. 10(b), and of the 4-level ISAC receiver in Fig. 11(a) and Fig. 11(b). The simulation results show that minimum BER and MSE of the 3-level receiver are located near the theoretical optimal value $|c_{2,\text{opt}}| = 0.610$, and those of the 4-level receiver appear near $|c_{2,\text{opt}}| = 0.982$. It proves that the design of the optimal quantization thresholds can minimize the performance loss brought by the low-resolution quantization.

Because of the large bandwidth of pulsed signals, the pulse-based ISAC systems should coexist with the existing radio systems with relatively narrow bandwidth. The signals radiated by narrowband radio systems are considered as NBI in the view of pulse-based ISAC systems. Considering that there exists the unknown NBI, the filtered received signal can be given by

$$r_{\text{fn}}(t) = r_{\text{f}}(t) + r_{\text{I}}(t), \tag{56}$$

where $r_{\text{I}}(t)$ is the filtered NBI.

In Fig. 12(a) and Fig. 12(b), we study the impact of NBI on the proposed ISAC systems. The NBI is modeled as a binary phase-shift keying (BPSK) modulation signal with center frequency $F_{\text{c}} = 5\text{GHz}$ and bit rate $R_{\text{NBI}} = 100\text{Kbit/s}$ [61], [62]. The signal-to-interference ratio (SIR) is defined as

$$\text{SIR} = \frac{\int_0^{T_{\text{s}}} p_{\text{f}}^2(t)dt}{\int_0^{T_{\text{s}}} r_{\text{I}}^2(t)dt}. \tag{57}$$

The simulation results show that the full-resolution ISAC receiver with no NBI has a SNR gap within 0.5dB in BER at SIR=-10dB and 1dB in MSE at SIR=-20dB. Clearly, BER and MSE will increase when SIR decreases, and the communication system is more sensitive to NBI than
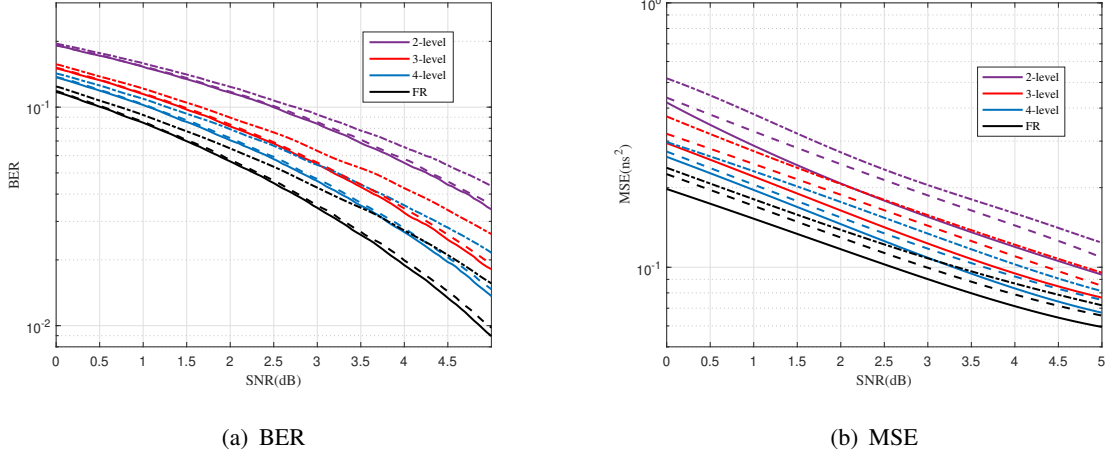
(a) BER

(b) MSE

Fig. 12. BER and MSE performance of the pulsed-based ISAC receiver at and various SIR and $N_{\mathrm{p}} = 3000$ (No NBI denoted as solid lines, SIR$= -5$dB denoted as dash lines and SIR$= -10$dB denoted as dash-dotted lines)

ranging. Generally, from simulation, when SIR is controlled more than -10dB, the performance loss caused by NBI is limited within 1dB SNR loss.

The correlation of sample points caused by high-speed sampling may also have an impact on the proposed ISAC systems. Considering the sampling interval of sample points used for ranging (i.e. $\mathbf{r}_{\mathrm{p,row}}^{(i)}$) is large enough to ignore the correlation of sample points, we only need to consider the communication system. In Appendix F, it is shown that when the Nyquist sampling rate $\mu = 2$ is adopted, all the sample points are independent. Considering the imperfect sampling clock or oversampling (i.e. $2 \leq \mu \leq 4$), the correlated random variable sequence $\mathbf{r}_{\mathrm{d,col}}^{(k_{\mathrm{d}})}$ can be modeled as a m-dependent Gaussian random variable sequence (defined in Appendix F), whose autocovariance matrix $\mathrm{cov}(\mathbf{r}_{\mathrm{d,col}}^{(k_{\mathrm{d}})})$ is given by

$$
\mathrm{cov}(\mathbf{r}_{\mathrm{d,col}}^{(k_{\mathrm{d}})}) = \begin{bmatrix} \sigma_{\mathrm{n}}^2 & \sigma_{\mathrm{cov}} & 0 & \dots & 0 & 0 \\ \sigma_{\mathrm{cov}} & \sigma_{\mathrm{n}}^2 & \sigma_{\mathrm{cov}} & \dots & 0 & 0 \\ \vdots & \ddots & \vdots & \vdots & \ddots & \vdots \\ 0 & 0 & 0 & \dots & \sigma_{\mathrm{cov}} & \sigma_{\mathrm{n}}^2 \end{bmatrix}, \tag{58}
$$

where σ_{cov} is the covariance of two adjacent samples.

The impact of the correlation on the BER of the full-resolution receiver and M-level ISAC receiver at $N_{\mathrm{p}} = 3000$ is shown in the Fig. 13. The 3-level ISAC receiver, for example, has about 0.5dB and 1dB SNR gap compared with $\sigma_{\mathrm{cov}} = 0$ at $\sigma_{\mathrm{cov}} = 0.1$ and $\sigma_{\mathrm{cov}} = 0.2$ respectively. Although the performance loss cause by the correlation of sample point is inevitable, it can be limited within 1dB SNR loss by adopting an appropriate sampling rate $2 \leq \mu \leq 4$.
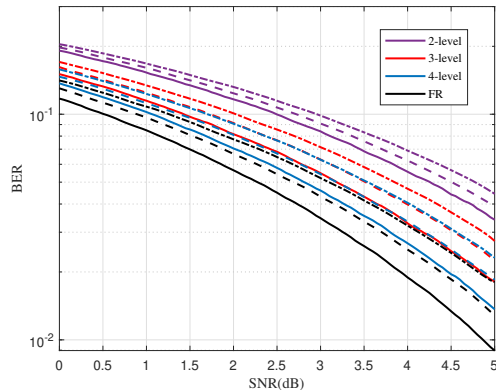
Fig. 13. BER performance of the pulsed-based ISAC receiver at and various covariance and $N_{\mathrm{p}} = 3000$ (σ_{n}^2 normalized to 1, $\sigma_{\mathrm{cov}} = 0$ denoted as solid lines, $\sigma_{\mathrm{cov}} = 0.1$ denoted as dash lines and $\sigma_{\mathrm{cov}} = 0.2$ denoted as dash-dotted lines)

VI. CONCLUSION

In this paper, we have proposed a full-resolution pulse-based ISAC receiver for multi-path channels. The proposed receiver can obtain the diversity gain of multi-path components to recover data symbols, and pick up the first path in the presence of multi-path components and AWGN by a threshold detection method based on NP rule. To reduce the cost of the high-speed full-resolution ADC, we have proposed a pulse-based ISAC receiver using a low-resolution ADC. The optimal quantization thresholds of the low-resolution ADC have also been obtained. Based on simulation results, we have shown that compared with the GML-based receiver, the proposed full-resolution ISAC receiver has 1dB SNR loss in BER and almost the same MSE performance with lower computational complexity, and compared with the full-resolution ISAC receiver, the SNR loss of the 3-level ISAC receiver is about 0.8dB in BER and 1dB in MSE but the ADC cost is significantly reduced.

APPENDIX A

THE PROOF OF PROPOSITION 1

We first denote the channel estimation error as $\tilde{\mathbf{w}} = \hat{\mathbf{w}} - \mathbf{w} = [\tilde{w}_0, \tilde{w}_1, ..., \tilde{w}_{N_{\mathrm{s}}-1}]^T$. From (8), we know that $\hat{\mathbf{w}} \sim \mathcal{CN}(\mathbf{w}, \frac{\sigma_{\mathrm{n}}^2}{N_{\mathrm{p}}}\mathbf{I}_{N_{\mathrm{s}}})$ by the sum of Gaussian random variables $r_{\mathrm{p}}^{(i,k_{\mathrm{p}})}$. Considering the channel estimation error $\tilde{\mathbf{w}}$, the symbol detector (11) can be written as

$$C_{\text{full}}(\boldsymbol{r}_{\text{d,col}}^{(k_{\text{d}})}, \hat{\mathbf{w}}) = \sum_{i=0}^{N_{\text{s}}-1} \left[(b_{k_{\text{d}}} w_i + n_{\text{d}}^{(i,k_{\text{d}})})(w_i + \tilde{w}_i) \right]$$

$$= \sum_{i=0}^{N_{\text{s}}-1} (b_{k_{\text{d}}} w_i^2 + b_{k_{\text{d}}} w_i \tilde{w}_i + n_{\text{d}}^{(i,k_{\text{d}})} w_i + n_{\text{d}}^{(i,k_{\text{d}})} \tilde{w}_i). \tag{59}$$

$C_{\text{full}}(\boldsymbol{r}_{\text{d,col}}^{(k_{\text{d}})}, \hat{\mathbf{w}})$ is a non-Gaussian random variable. Thanks to the broadband of pulsed signal and Nyquist sampling theorem, N_{s} should be very large. Thus, the only non-Gaussian term $\sum_{i=0}^{N_{\text{s}}-1} n_{\text{d}}^{(i,k_{\text{d}})} \tilde{w}_i$ of (59) can be approximated as a Gaussian random variable by using the central limit theorem, and $C_{\text{full}}(\boldsymbol{r}_{\text{d,col}}^{(k_{\text{d}})}, \hat{\mathbf{w}})$ can be approximated to a Gaussian distribution in large samples case. The BER performance is estimated as $Q(d_{\min}/\sqrt{4\sigma_{\text{eq}}^2})$ [56], where $d_{\min} = 2\text{E}[C_{\text{full}}(\boldsymbol{r}_{\text{d,col}}^{(k_{\text{d}})}, \hat{\mathbf{w}})|b_{k_{\text{d}}} = 1]$ denotes the equivalent Euclidean distance between two constellation symbols, and $\sigma_{\text{eq}}^2 = \text{var}[C_{\text{full}}(\boldsymbol{r}_{\text{d,col}}^{(k_{\text{d}})}, \hat{\mathbf{w}})|b_{k_{\text{d}}} = 1]$ denotes the equivalent noise variance. The expectation of $C_{\text{full}}(\boldsymbol{r}_{\text{d,col}}^{(k_{\text{d}})}, \hat{\mathbf{w}})$ when $b_{k_{\text{d}}} = 1$ is given by

$$\text{E}[C_{\text{full}}(\boldsymbol{r}_{\text{d,col}}^{(k_{\text{d}})}, \hat{\mathbf{w}})|b_{k_{\text{d}}} = 1] = \sum_{i=0}^{N_{\text{s}}-1} w_i^2. \tag{60}$$

Then, the variance of $C_{\text{full}}(\boldsymbol{r}_{\text{d,col}}^{(k_{\text{d}})}, \hat{\mathbf{w}})$ when $b_{k_{\text{d}}} = 1$ is given by

$$\text{var}[C_{\text{full}}(\boldsymbol{r}_{\text{d,col}}^{(k_{\text{d}})}, \hat{\mathbf{w}})|b_{k_{\text{d}}} = 1] = \sum_{i=0}^{N_{\text{s}}-1} w_i^2 \sigma_{\text{n}}^2 + \frac{\sigma_{\text{n}}^2}{N_{\text{p}}} \sum_{i=0}^{N_{\text{s}}-1} (w_i^2 + \sigma_{\text{n}}^2). \tag{61}$$

Taking (60) and (61) into the calculation of BER, we can evaluate $P_{\text{e,full}}$ as

$$P_{\text{e,full}} \approx Q \left(\sqrt{\frac{\frac{E_{\text{s}}}{\sigma_{\text{n}}^2}}{1 + \frac{N_{\text{s}}}{N_{\text{p}}} \left(\frac{E_{\text{s}}}{\sigma_{\text{n}}^2}\right)^{-1}}} \right) (as\ N_{\text{s}} > N_{\text{p}} \gg 1)$$

$$= Q \left(\sqrt{\frac{2\mu\text{SNR}}{1 + \frac{N_{\text{s}}}{N_{\text{p}}}(2\mu\text{SNR})^{-1}}} \right), \tag{62}$$

where

$$E_{\text{s}} = \sum_{i=0}^{N_{\text{s}}-1} w_i^2 = \frac{1}{T_{\text{sam}}} \int_{-\infty}^{+\infty} p_{\text{f}}^2(t) dt. \tag{63}$$

APPENDIX B

THE PROOF OF PROPOSITION 2

Because there is a linear relationship between D and τ_1, $\text{CRLB}_{D,\text{full}} = c^2 \cdot \text{CRLB}_{\tau_1,\text{full}}$. We first obtain Fisher information matrix (FIM) of $\boldsymbol{\theta}$ to calculate $\text{CRLB}_{\tau_1,\text{full}}$, where $\boldsymbol{\theta} =$

$[\tau_1, h_1, ..., \tau_L, h_L]^T$ is a vector of unknown parameters of the multi-path channel. It is very complicated to compute $\mathbf{F}_{\boldsymbol{\theta}}$ directly. Thus, we can use the reparametrization of FIM [63] to evaluate $\mathbf{F}_{\boldsymbol{\theta}}$ as

$$\mathbf{F}_{\boldsymbol{\theta}} = \left(\frac{\partial \mathbf{w}^T}{\partial \boldsymbol{\theta}}\right) \mathbf{F}_{\mathbf{w}} \left(\frac{\partial \mathbf{w}^T}{\partial \boldsymbol{\theta}}\right)^T, \tag{64}$$

where

$$\mathbf{F}_{\mathbf{w}} = \mathrm{E}\left[\left(\frac{\partial}{\partial \mathbf{w}} \ln \mathrm{Pr}(\mathbf{R}_{\mathrm{p}}|\mathbf{a}, \mathbf{w})\right)\left(\frac{\partial}{\partial \mathbf{w}} \ln \mathrm{Pr}(\mathbf{R}_{\mathrm{p}}|\mathbf{a}, \mathbf{w})\right)^T\right]. \tag{65}$$

Note that $\mathrm{Pr}(\mathbf{R}_{\mathrm{p}}|\mathbf{a}, \mathbf{w}) = \prod_{i=0}^{N_{\mathrm{s}}-1} \prod_{k_{\mathrm{p}}=0}^{N_{\mathrm{p}}-1} \mathrm{Pr}(r_{\mathrm{p}}^{(i,k_{\mathrm{p}})}|a_{k_{\mathrm{p}}}, w_i)$ with $\mathrm{Pr}(r_{\mathrm{p}}^{(i,k_{\mathrm{p}})}|a_{k_{\mathrm{p}}}, w_i) = f_{\mathrm{n}}(r_{\mathrm{p}}^{(i,k_{\mathrm{p}})} - a_{k_{\mathrm{p}}} w_i)$. The each entry of $\mathbf{F}_{\mathbf{w}}$ is evaluated as

$$\mathrm{E}\left[\frac{\partial^2}{\partial w_i \partial w_j} \ln \mathrm{Pr}(\mathbf{R}_{\mathrm{p}}|\mathbf{a}, \mathbf{w})\right] = 0,$$

$$\mathrm{E}\left[\frac{\partial^2}{\partial w_i^2} \ln \mathrm{Pr}(\mathbf{R}_{\mathrm{p}}|\mathbf{a}, \mathbf{w})\right] = -\frac{N_{\mathrm{p}}}{\sigma_{\mathrm{n}}^2}. \tag{66}$$

$$i, j = 0, 1, \ \ldots \ , N_{\mathrm{s}} - 1 \quad i \neq j$$

Then, taking (66) into (65), $\mathbf{F}_{\mathbf{w}}$ can be evaluated as

$$\mathbf{F}_{\mathbf{w}} = \frac{N_{\mathrm{p}}}{\sigma_{\mathrm{n}}^2} \mathbf{I}_{N_{\mathrm{s}}}. \tag{67}$$

Then, we can evaluate $\frac{\partial \mathbf{w}^T}{\partial \boldsymbol{\theta}}$ as

$$\frac{\partial \mathbf{w}^T}{\partial \boldsymbol{\theta}} = \begin{bmatrix} -h_1 \dot{p}_{\mathrm{r}}(T_{\mathrm{sam}} - \tau_1) & \ldots & -h_1 \dot{p}_{\mathrm{r}}(N_{\mathrm{s}} T_{\mathrm{sam}} - \tau_1) \\ p_{\mathrm{r}}(T_{\mathrm{sam}} - \tau_1) & \ldots & p_{\mathrm{r}}(N_{\mathrm{s}} T_{\mathrm{sam}} - \tau_1) \\ \vdots & \ddots & \vdots \\ -h_L \dot{p}_{\mathrm{r}}(T_{\mathrm{sam}} - \tau_L) & \ldots & -h_L \dot{p}_{\mathrm{r}}(N_{\mathrm{s}} T_{\mathrm{sam}} - \tau_L) \\ p_{\mathrm{r}}(T_{\mathrm{sam}} - \tau_L) & \ldots & p_{\mathrm{r}}(N_{\mathrm{s}} T_{\mathrm{sam}} - \tau_L) \end{bmatrix}, \tag{68}$$

where $\dot{p}_{\mathrm{r}}(t) = \frac{\partial p_{\mathrm{r}}(t)}{\partial t}$. Taking (67) and (68) into (64), we can evaluate $2L \times 2L$ FIM $\mathbf{F}_{\boldsymbol{\theta}}$ as

$$\mathbf{F}_{\boldsymbol{\theta}} = \frac{N_{\mathrm{p}}}{\sigma_{\mathrm{n}}^2} \begin{bmatrix} h_1^2 \ddot{P}_{1,1} & h_1 \dot{P}_{1,1} & \ldots & h_1 h_L \ddot{P}_{1,L} & h_1 \dot{P}_{1,L} \\ h_1 \dot{P}_{1,1} & P_{1,1} & \ldots & h_L \dot{P}_{L,1} & P_{1,L} \\ \vdots & \vdots & \ddots & \vdots & \vdots \\ h_1 h_L \ddot{P}_{1,L} & h_L \dot{P}_{L,1} & \ldots & h_L^2 \ddot{P}_{L,L} & h_L \dot{P}_{L,L} \\ h_1 \dot{P}_{1,L} & P_{1,L} & \ldots & h_L \dot{P}_{L,L} & P_{L,L} \end{bmatrix}, \tag{69}$$

where

$$\ddot{P}_{l,l'} = \sum_{i=1}^{N_{\mathrm{s}}} \dot{p}_{\mathrm{r}}(iT_{\mathrm{sam}} - \tau_l)\dot{p}_{\mathrm{r}}(iT_{\mathrm{sam}} - \tau_{l'}),$$

$$\dot{P}_{l,l'} = -\sum_{i=1}^{N_{\mathrm{s}}} \dot{p}_{\mathrm{r}}(iT_{\mathrm{sam}} - \tau_l)p_{\mathrm{r}}(iT_{\mathrm{sam}} - \tau_{l'}), \tag{70}$$

$$P_{l,l'} = \sum_{i=1}^{N_{\mathrm{s}}} p_{\mathrm{r}}(iT_{\mathrm{sam}} - \tau_l)p_{\mathrm{r}}(iT_{\mathrm{sam}} - \tau_{l'}).$$

Because our goal is to estimate τ_1, $\boldsymbol{\theta}$ can be divided into two part: $\boldsymbol{\theta} = [\tau_1, \bar{\boldsymbol{\theta}}]$, where $\bar{\boldsymbol{\theta}}$ is the parameter vector without the need to be estimated. $\mathbf{F}_{\boldsymbol{\theta}}$ can be rewritten as

$$\mathbf{F}_{\boldsymbol{\theta}} = \frac{N_{\mathrm{p}}}{\sigma_{\mathrm{n}}^2} \begin{bmatrix} h_1^2 \ddot{P}_{1,1} & \mathbf{F}_{\tau_1 \bar{\boldsymbol{\theta}}} \\ \mathbf{F}_{\tau_1 \bar{\boldsymbol{\theta}}}^T & \mathbf{F}_{\bar{\boldsymbol{\theta}}} \end{bmatrix}, \tag{71}$$

where $\mathbf{F}_{\tau_1 \bar{\boldsymbol{\theta}}}$ and $\mathbf{F}_{\bar{\boldsymbol{\theta}}}$ contain the Fisher information of $\bar{\boldsymbol{\theta}}$. $\mathbf{F}_{\tau_1}$ is the Fisher information of τ_1, and can be calculated by the Schur complement of $\mathbf{F}_{\bar{\boldsymbol{\theta}}}$. That is,

$$\mathbf{F}_{\tau_1} = \frac{N_{\mathrm{p}}}{\sigma_{\mathrm{n}}^2}(h_1^2 \ddot{P}_{1,1} - \mathbf{F}_{\tau_1 \bar{\boldsymbol{\theta}}} \mathbf{F}_{\bar{\boldsymbol{\theta}}}^{-1} \mathbf{F}_{\tau_1 \bar{\boldsymbol{\theta}}}^T). \tag{72}$$

Thus, the CRLB of τ_1 is evaluated as

$$\mathrm{CRLB}_{\tau_1,\mathrm{full}} = \mathbf{F}_{\tau_1}^{-1} = \frac{\sigma_{\mathrm{n}}^2}{(1 - \eta)N_{\mathrm{p}}h_1^2 \ddot{P}_{1,1}}, \tag{73}$$

where

$$\eta = \frac{\mathbf{F}_{\tau_1 \bar{\boldsymbol{\theta}}} \mathbf{F}_{\bar{\boldsymbol{\theta}}}^{-1} \mathbf{F}_{\tau_1 \bar{\boldsymbol{\theta}}}^T}{h_1^2 \ddot{P}_{1,1}} \tag{74}$$

represents the influence coefficient of the unknown nuisance parameter vector $\bar{\boldsymbol{\theta}}$. Because $\mathbf{F}_{\tau_1 \bar{\boldsymbol{\theta}}} \mathbf{F}_{\bar{\boldsymbol{\theta}}}^{-1} \mathbf{F}_{\tau_1 \bar{\boldsymbol{\theta}}}^T \geq 0$ ($\mathbf{F}_{\bar{\boldsymbol{\theta}}}$ is positive-semidefinite) and $\mathbf{F}_{\tau_1} \geq 0$, $\eta \in [0, 1]$. Then, with some manipulations, we can transform $\mathrm{CRLB}_{\tau_1,\mathrm{full}}$ into a familiar form. Because $T_{\mathrm{s}} \gg T_{\mathrm{sam}}$, $\frac{h_1^2 \ddot{P}_{1,1}}{\sigma_n^2}$ can be evaluated as

$$\begin{aligned} \frac{h_1^2 \ddot{P}_{1,1}}{\sigma_n^2} &\approx \frac{h_1^2}{T_{\mathrm{sam}}\sigma_n^2} \int_0^{T_{\mathrm{s}}} \dot{p}_{\mathrm{r}}(t)^2 dt \\ &= \frac{8\pi^2 \mu h_1^2}{N_0} \int_{-\infty}^{+\infty} f^2 |P_{\mathrm{r}}(f)^2| df \\ &= 8\mu\pi^2 \frac{\int_{-\infty}^{+\infty} h_1^2 |P_{\mathrm{r}}(f)^2| df}{N_0} \cdot \frac{\int_{-\infty}^{+\infty} f^2 \cdot |P_{\mathrm{r}}(f)^2| df}{\int_{-\infty}^{+\infty} |P_{\mathrm{r}}(f)^2| df} \\ &= 8\pi^2 \beta^2 \mu \mathrm{SNP}_{\mathrm{p}}. \end{aligned} \tag{75}$$

The second step is due to $\sigma_{\mathrm{n}}^2 T_{\mathrm{sam}} = N_0 B T_{\mathrm{sam}} = \frac{N_0}{2\mu}$. Taking (75) into (73), $\mathrm{CRLB}_{\tau_1,\mathrm{full}}$ can be expressed as

$$\mathrm{CRLB}_{\tau_1,\mathrm{full}} = \mathbf{F}_{\tau_1}^{-1} = \frac{1}{8\pi^2(1 - \eta)N_{\mathrm{p}}\beta^2 \mu \mathrm{SNR}_{\mathrm{p}}}. \tag{76}$$

Then, $\text{CRLB}_{D,\text{full}}$ is given by

$$\text{CRLB}_{D,\text{full}} = \frac{c^2}{8\pi^2(1-\eta)N_{\text{p}}\beta^2\mu\text{SNR}_{\text{p}}}. \tag{77}$$

APPENDIX C

THE PROOF OF LEMMA 1

Because $\hat{\mathbf{w}}$ is a non-Gaussian random vector with unknown distribution, it is hard to analyze the effect of the channel estimation error on the data recovery. Thus, we hope to obtain the asymptotic PDF of $\hat{\mathbf{w}}$ under the condition of the large samples (i.e. $N_{\text{p}} \gg 1$). According to [64], $\hat{\mathbf{w}}$ is asymptotically distributed according to

$$\hat{\mathbf{w}} \sim \mathcal{CN}(\mathbf{w}, \mathbf{F}_{\mathbf{w}}^{-1}). \tag{78}$$

The fitting conditions of (78) are the existence of the first order and second order derivatives of the log-likelihood function and Fisher information being nonzero. Note that $\Pr(x_{\text{p}}^{(i,k_{\text{p}})} = l_m|a_{k_{\text{p}}}, w_i) = F_{\text{n}}(c_m - a_{k_{\text{p}}}w_i) + F_{\text{n}}(c_{m-1} - a_{k_{\text{p}}}w_i)$ with $a_{k_{\text{p}}}$ being a known symbol. It can be easily proved that the derivatives of $\ln\Pr(x_{\text{p}}^{(i,k_{\text{p}})} = l_m|a_{k_{\text{p}}}, w_i)$ can be well defined. Then, we evaluate the value of $\mathbf{F}_{\mathbf{w}}$ as

$$\mathbf{F}_{\mathbf{w}} = \text{E}\left[\left(\frac{\partial}{\partial\mathbf{w}}\ln\Pr(\mathbf{X}_{\text{p}}|\mathbf{a},\mathbf{w})\right)\left(\frac{\partial}{\partial\mathbf{w}}\ln\Pr(\mathbf{X}_{\text{p}}|\mathbf{a},\mathbf{w})\right)^T\right]. \tag{79}$$

Note that $\Pr(\mathbf{X}_{\text{p}}|\mathbf{a},\mathbf{w}) = \prod_{i=0}^{N_{\text{s}}-1}\prod_{k_{\text{p}}=0}^{N_{\text{p}}-1}\Pr(x_{\text{p}}^{(i,k_{\text{p}})}|a_{k_{\text{p}}}, w_i)$, with $\Pr(x_{\text{p}}^{(i,k_{\text{p}})} = l_{\overline{m}_{i,k_{\text{p}}}}|a_{k_{\text{p}}}, w_i) = F_{\text{n}}(c_{\overline{m}_{i,k_{\text{p}}}} - a_{k_{\text{p}}}w_i) - F_{\text{n}}(c_{\overline{m}_{i,k_{\text{p}}}-1} - a_{k_{\text{p}}}w_i)$. The each entry of $\mathbf{F}_{\mathbf{w}}$ is evaluated as

$$\text{E}\left[\frac{\partial^2}{\partial w_i\partial w_j}\ln\Pr(\mathbf{X}_{\text{p}}|\mathbf{a},\mathbf{w})\right] = 0,$$

$$\text{E}\left[\frac{\partial^2}{\partial w_i^2}\ln\Pr(\mathbf{X}_{\text{p}}|\mathbf{a},\mathbf{w})\right] = -\frac{N_{\text{p}}\alpha_{w_i}}{\sigma_{\text{n}}^2}. \tag{80}$$

$$i, j = 0, 1, \ldots, N_{\text{p}}-1 \quad i \neq j$$

Finally, taking (80) into (79) and performing a matrix inversion, we have

$$\mathbf{F}_{\mathbf{w}}^{-1} = \frac{\sigma_{\text{n}}^2}{N_{\text{p}}} \cdot \text{diag}\{\alpha_{w_0}^{-1}, \alpha_{w_1}^{-1}, \ldots, \alpha_{w_{N_{\text{s}}-1}}^{-1}\}. \tag{81}$$

APPENDIX D

THE PROOF OF PROPOSITION 3

In Lemma 1, we obtain the asymptotic PDF of the channel estimation error $\tilde{\mathbf{w}}$. Considering the effect of $\tilde{\mathbf{w}}$, the symbol detector (32) can be rewritten as

$$C_{\text{low}}(\mathbf{x}_{\text{d,col}}^{(k_{\text{d}})}, \hat{\mathbf{w}}) = \sum_{i=0}^{N_{\text{s}}-1}(w_i + \tilde{w}_i)\frac{f_{\text{n}}(c_{m_{i,k_{\text{d}}}-1}) - f_{\text{n}}(c_{m_{i,k_{\text{d}}}})}{F_{\text{n}}(c_{m_{i,k_{\text{d}}}}) - F_{\text{n}}(c_{m_{i,k_{\text{d}}}-1})}. \tag{82}$$

It is proved in [65] that the LLR can be approximated as a Gaussian random variable in multi-path channels. Due to the large delay spread of the multi-path channel, the number of samples N_{s} is very large. It makes relatively large samples (more than 10) share a similar signal strength w_i. We can use the central limit theorem to approximate the sum of these samples as a Gaussian random variable, and then LLR can also be approximated to a Gaussian distribution by adding up such approximate Gaussian random variables. BER can be evaluated as $Q(d_{\min}/\sqrt{4\sigma_{\mathrm{eq}}^2})$, where $d_{\min} = 2\mathrm{E}[C_{\mathrm{low}}(\mathbf{x}_{\mathrm{d,col}}^{(k_{\mathrm{d}})}, \hat{\mathbf{w}})|b_{k_{\mathrm{d}}} = 1]$ and $\sigma_{\mathrm{eq}}^2 = \mathrm{var}[C_{\mathrm{low}}(\mathbf{x}_{\mathrm{d,col}}^{(k_{\mathrm{d}})}, \hat{\mathbf{w}})|b_{k_{\mathrm{d}}} = 1]$. At first, we can evaluate $d_{\min}$ as

$$
\begin{aligned}
d_{\min} &= 2\mathrm{E}[C_{\mathrm{low}}(\mathbf{x}_{\mathrm{d,col}}^{(k_{\mathrm{d}})}, \hat{\mathbf{w}})|b_{k_{\mathrm{d}}} = 1] \\
&= \frac{2}{\sigma_{\mathrm{n}}^2} \sum_{i=0}^{N_{\mathrm{s}}-1} w_i^2 \sum_{m=1}^{M} \frac{\left(\phi(\frac{c_m}{\sigma_{\mathrm{n}}}) - \phi(\frac{c_{m-1}}{\sigma_{\mathrm{n}}})\right)^2}{\Phi(\frac{c_{m-1}}{\sigma_{\mathrm{n}}}) - \Phi(\frac{c_{m-1}}{\sigma_{\mathrm{n}}})} \\
&= 4\alpha_0 \cdot \mu\mathrm{SNR},
\end{aligned}
\tag{83}
$$

where α_0 is the quantization efficiency at $w_i = 0$. Then, we can evaluate σ_{eq}^2 as

$$
\begin{aligned}
\sigma_{\mathrm{eq}}^2 &= \mathrm{var}[C_{\mathrm{low}}(\mathbf{x}_{\mathrm{d,col}}^{(k_{\mathrm{d}})}, \hat{\mathbf{w}})|b_{k_{\mathrm{d}}} = 1] \\
&= \sum_{i=0}^{N_{\mathrm{s}}-1} \mathrm{var}[\hat{w}_i]\mathrm{E}[(x_{\mathrm{d}}^{(i,k_{\mathrm{d}})})^2|b_{k_{\mathrm{d}}} = 1] + \sum_{i=0}^{N_{\mathrm{s}}-1} \mathrm{var}[x_{\mathrm{d}}^{(i,k_{\mathrm{d}})}|b_{k_{\mathrm{d}}} = 1]\mathrm{E}[\hat{w}_i]^2.
\end{aligned}
\tag{84}
$$

Then, (84) can be divided into two terms. The first term can be evaluated as

$$
\begin{aligned}
\sum_{i=0}^{N_{\mathrm{s}}-1} \mathrm{var}[x_{\mathrm{d}}^{(i,k_{\mathrm{d}})}|b_{k_{\mathrm{d}}} = 1]\mathrm{E}[\hat{w}_i]^2 &= \sum_{i=0}^{N_{\mathrm{s}}-1} w_i^2 \left[\sum_{m=1}^{M} l_m^2 f_m^{(i,k_{\mathrm{d}})} - \left(\sum_{m=1}^{M} l_m f_m^{(i,k_{\mathrm{d}})}\right)^2\right] \\
&= \frac{\alpha_0}{\sigma_{\mathrm{n}}^2} \sum_{i=0}^{N_{\mathrm{s}}-1} w_i^2 + \frac{\alpha_0^2}{\sigma_{\mathrm{n}}^4} \sum_{i=0}^{N_{\mathrm{s}}-1} w_i^4 \\
&= 2\alpha_0 \cdot \mu\mathrm{SNR} + \frac{4\alpha_0^2\mu^2 T_{\mathrm{sam}}}{N_0^2} \cdot \int_{-\infty}^{+\infty} p_{\mathrm{f}}^4(t)dt \\
&\approx 2\alpha_0 \cdot \mu\mathrm{SNR}. \quad (\text{as } \mathrm{T_{sam}} \to +\infty)
\end{aligned}
\tag{85}
$$

The second term can be evaluated as

$$
\begin{aligned}
\sum_{i=0}^{N_{\mathrm{s}}-1} \mathrm{var}[\hat{w}_i]\mathrm{E}[(x_{\mathrm{d}}^{(i,k_{\mathrm{d}})})^2|b_{k_{\mathrm{d}}} = 1] &= \sum_{i=0}^{N_{\mathrm{s}}-1} \frac{\sigma_{\mathrm{n}}^2}{N_{\mathrm{p}}\alpha_{w_i}} \sum_{m=1}^{M} l_m^2 f_m^{(i,k_{\mathrm{d}})} \\
&= \sum_{i=0}^{N_{\mathrm{s}}-1} \frac{\sigma_{\mathrm{n}}^2}{N_{\mathrm{p}}\alpha_{w_i}} \sum_{m=1}^{M} \frac{(f_{\mathrm{n}}(c_m) - f_{\mathrm{n}}(c_{m-1}))^2}{F_{\mathrm{n}}(c_m) - F_{\mathrm{n}}(c_{m-1})} \\
&= \sum_{i=0}^{N_{\mathrm{s}}-1} \frac{\alpha_0}{N_{\mathrm{p}}\alpha_{w_i}} \\
&\approx \frac{N_{\mathrm{s}}}{N_{\mathrm{p}}}.
\end{aligned}
\tag{86}
$$

Because pulsed signals has the low duty-cycle (i.e. the large percentage of sample points satisfies $w_i = 0$) and the ISAC system works in a weak signal case, $\sum_{i=0}^{N_s-1} \frac{\alpha_0}{\alpha_{w_i}} \approx N_s$ can be workable and substituted in (86). Taking (85) and (86) into (84), (84) can be written as

$$\sigma_{\text{eq}}^2 = 2\alpha_0 \cdot \mu\text{SNR} + \frac{N_s}{N_p}. \tag{87}$$

Finally, we can evaluate $P_{\text{e,low}}$ as

$$P_{\text{e,low}} = Q\left(\sqrt{\frac{2\alpha_0 \cdot \mu\text{SNR}}{1 + \frac{N_s}{N_p}(2\alpha_0 \cdot \mu\text{SNR})^{-1}}}\right). \tag{88}$$

We remark that the conclusions can be obtained under the condition of low SNR. When SNR is high, our approximation is not accurate. However, the inaccuracy of approximation can be ignored, because the performance of ISAC system is dominated by deep fading channel in which useful signals are submerged in noise. Therefore, the low SNR case is reasonably assumed.

APPENDIX E
THE PROOF OF PROPOSITION 4

Similar to Appendix B, we first obtain the FIM $\mathbf{F}_{\boldsymbol{\theta}}$ by the reparametrization of FIM mentioned in (64). $\mathbf{F_w}$ has been calculated in Appendix C. Taking (68) and (81) into (64), we can evaluate $\mathbf{F}_{\boldsymbol{\theta}}$ as

$$\mathbf{F}_{\boldsymbol{\theta}} = \frac{N_p}{\sigma_n^2} \begin{bmatrix} h_1^2 \ddot{Q}_{1,1} & h_1 \dot{Q}_{1,1} & \ldots & h_1 h_L \ddot{Q}_{1,L} & h_1 \dot{Q}_{1,L} \\ h_1 \dot{Q}_{1,1} & Q_{1,1} & \ldots & h_L \dot{Q}_{L,1} & Q_{1,L} \\ \vdots & \vdots & \ddots & \vdots & \vdots \\ h_1 h_L \ddot{Q}_{1,L} & h_L \dot{Q}_{L,1} & \ldots & h_L^2 \ddot{Q}_{L,L} & h_L \dot{Q}_{L,L} \\ h_1 \dot{Q}_{1,L} & Q_{1,L} & \ldots & h_L \dot{Q}_{L,L} & Q_{L,L} \end{bmatrix}, \tag{89}$$

where

$$\ddot{Q}_{l,l'} = \sum_{i=1}^{N_s} \alpha_{w_i} \dot{p}_r(iT_{\text{sam}} - \tau_l)\dot{p}_r(iT_{\text{sam}} - \tau_{l'}),$$

$$\dot{Q}_{l,l'} = -\sum_{i=1}^{N_s} \alpha_{w_i} \dot{p}_r(iT_{\text{sam}} - \tau_l)p_r(iT_{\text{sam}} - \tau_{l'}), \tag{90}$$

$$Q_{l,l'} = \sum_{i=1}^{N_s} \alpha_{w_i} p_r(iT_{\text{sam}} - \tau_l)p_r(iT_{\text{sam}} - \tau_{l'}).$$

Considering $\boldsymbol{\theta} = [\tau_1, \bar{\boldsymbol{\theta}}]$, $\mathbf{F}_{\boldsymbol{\theta}}$ can be rewritten as

$$\mathbf{F}_{\boldsymbol{\theta}} = \frac{N_p}{\sigma_n^2} \begin{bmatrix} h_1^2 \ddot{Q}_{1,1} & \mathbf{F}_{\tau_1 \bar{\boldsymbol{\theta}}} \\ \mathbf{F}_{\tau_1 \bar{\boldsymbol{\theta}}}^T & \mathbf{F}_{\bar{\boldsymbol{\theta}}} \end{bmatrix}. \tag{91}$$
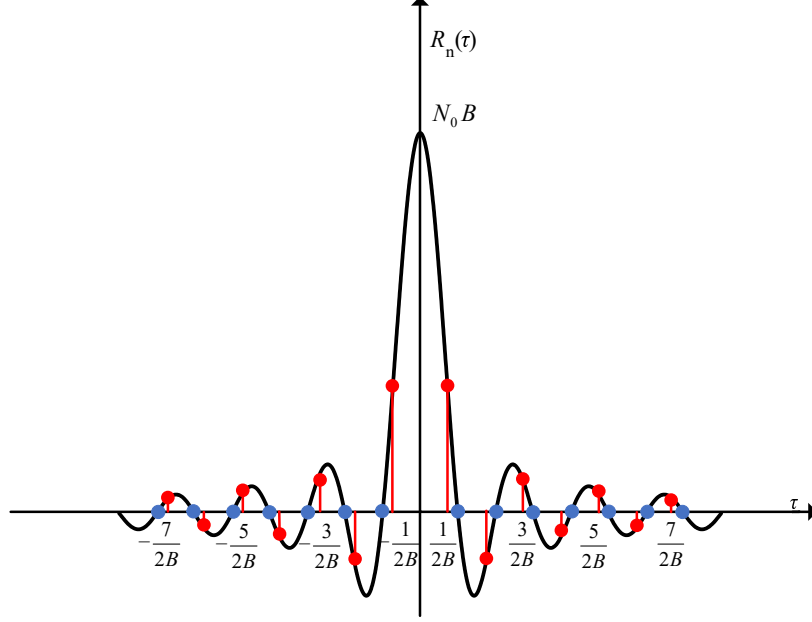
Fig. 14. The autocorrelation function of $n(t)$ with Nyquist sampling rate $T_{\text{sam}} = \frac{1}{2B}$ (denoted as blue points) and oversampling rate $T_{\text{sam}} \geq \frac{1}{2B}$ (denoted as red points)

Then, $\mathbf{F}_{\tau_1}$ can be evaluated as

$$\mathbf{F}_{\tau_1} = \frac{N_{\text{p}}}{\sigma_{\text{n}}^2}(h_1^2\ddot{Q}_{1,1} - \mathbf{F}_{\tau_1\bar{\theta}}\mathbf{F}_{\bar{\theta}}^{-1}\mathbf{F}_{\tau_1\bar{\theta}}^T). \tag{92}$$

Note that $\ddot{Q}_{1,1} \approx \sum_{i=1}^{N_{\text{s}}} \alpha_0 \dot{p}_{\text{r}}(iT_{\text{sam}} - \tau_l)\dot{p}_{\text{r}}(iT_{\text{sam}} - \tau_{l'}) = \alpha_0\ddot{P}_{1,1}$ in the low duty-cycle and weak signal case. From (75), $\text{CRLB}_{\tau_1,\text{low}}$ can be evaluated as

$$
\begin{aligned}
\text{CRLB}_{\tau_1,\text{low}} &= \mathbf{F}_{\tau_1}^{-1} \\
&= \frac{\sigma_{\text{n}}^2}{(1-\eta)N_{\text{p}}\alpha_0 h_1^2\ddot{P}_{1,1}} \\
&= \frac{1}{8\pi^2(1-\eta)N_{\text{p}}\beta^2\alpha_0\mu\text{SNR}_{\text{p}}}.
\end{aligned}
\tag{93}
$$

Then, $\text{CRLB}_{D,\text{low}}$ is given by

$$\text{CRLB}_{D,\text{low}} = \frac{c^2}{8\pi^2(1-\eta)N_{\text{p}}\beta^2\alpha_0\mu\text{SNR}_{\text{p}}}. \tag{94}$$

APPENDIX F

THE CORRELATION OF SAMPLE POINTS

At first, we will analyze the correlation function of sample points. In the proposed system, the received signal is firstly filtered by a ideal low-pass filter (LPF) of bandwidth B whose

frequency response can be given by

$$H(f) = \begin{cases} 1, & -B \leq f \leq B \\ 0, & \text{the other} \end{cases}. \tag{95}$$

From (3), $n(t)$ is the filtered additive white Gaussian noise (AWGN). The power spectral density function of $n(t)$ can be given by

$$S_{\mathrm{n}}(f) = |H(f)|^2 \cdot S_{\mathrm{AWGN}}(f) = \begin{cases} N_0/2, & -B \leq f \leq B \\ 0, & \text{the other} \end{cases}, \tag{96}$$

where

$$S_{\mathrm{AWGN}}(f) = N_0/2 \quad \forall f \tag{97}$$

is the power spectral density of AWGN. The autocorrelation function of $n(t)$ (denoted as $R_{\mathrm{n}}(\tau)$) can be obtained by the Fourier transform of $S_{\mathrm{n}}(f)$, That is

$$R_{\mathrm{n}}(\tau) = \frac{N_0 \sin(2\pi B \tau)}{2\pi \tau}. \tag{98}$$

In Fig. 14, it is shown that all the sample points are independent when the Nyquist sampling rate $\mu = 2$ is adopted. However, when the sampling rate increases, the correlation of sample points will brings the inevitable impact on the proposed ISAC system.

Considering that the offset of sampling frequency exists or the oversampling rate (i.e. $2 \leq \mu \leq 4$) is performed, the sample point sequence $\mathbf{r}_{\mathrm{d,col}}^{(k_{\mathrm{d}})} = [r_{\mathrm{d}}^{(0,k_{\mathrm{d}})}, r_{\mathrm{d}}^{(1,k_{\mathrm{d}})}, ..., r_{\mathrm{d}}^{(N_{\mathrm{s}}-1,k_{\mathrm{d}})}]^T$ can be modeled as a m-dependent Gaussian random variable sequence with $m = 1$ in which only the adjacent sample points are relevant. The autocovariance matrix $\mathrm{cov}(\mathbf{r}_{\mathrm{d,col}}^{(k_{\mathrm{d}})})$ of the m-dependent Gaussian random variable sequence when $m = 1$ can be given by (58). (58) can be valid under two certain assumptions: (1) all the sample points are only relevant to the nearest sample points. (2) the covariance of two adjacent samples is a fixed constant. The assumption (1) can be proved in Fig. 14. When $2 \leq \mu \leq 4$, only the nearest sample points are located in the main lobe, and the correlation with the other sample points lied in side lobes can be ignored. We assume that the sampling frequency offset is fixed for the duration of signal processing, and hence the assumption (2) can hold. The central limit theorem (CLT) of the m-dependent random variable sequence has been proved in [66], [67].

REFERENCES

[1] J. A. Zhang, F. Liu, C. Masouros, R. W. Heath, Z. Feng, L. Zheng, and A. Petropulu, "An overview of signal processing techniques for joint communication and radar sensing," *IEEE J. Sel. Topics Signal Process.*, vol. 15, no. 6, pp. 1295–1315, 2021.

[2] F. Liu, Y. Cui, C. Masouros, J. Xu, T. X. Han, Y. C. Eldar, and S. Buzzi, "Integrated sensing and communications: Towards dual-functional wireless networks for 6G and beyond," *IEEE J. Sel. Areas Commun.*, pp. 1–1, 2022.

[3] D. K. Pin Tan, J. He, Y. Li, A. Bayesteh, Y. Chen, P. Zhu, and W. Tong, "Integrated sensing and communication in 6G: Motivations, use cases, requirements, challenges and future directions," in *Proc. 1st IEEE Int. Online Symp. Joint Commun. Sens. (JC&S)*, 2021, pp. 1–6.

[4] L. Zheng, M. Lops, Y. C. Eldar, and X. Wang, "Radar and communication coexistence: An overview: A review of recent methods," *IEEE Signal Process. Mag.*, vol. 36, no. 5, pp. 85–99, 2019.

[5] M.-X. Gu, M.-C. Lee, Y.-S. Liu, and T.-S. Lee, "Design and analysis of frequency hopping-aided FMCW-based integrated radar and communication systems," *IEEE Trans. Commun.*, vol. 70, no. 12, pp. 8416–8432, 2022.

[6] D. Ma, N. Shlezinger, T. Huang, Y. Liu, and Y. C. Eldar, "FRaC: FMCW-based joint radar-communications system via index modulation," *IEEE J. Sel. Topics Signal Process.*, vol. 15, no. 6, pp. 1348–1364, 2021.

[7] C. Sturm and W. Wiesbeck, "Waveform design and signal processing aspects for fusion of wireless communications and radar sensing," *Proc. IEEE*, vol. 99, no. 7, pp. 1236–1259, 2011.

[8] X. Chen, Z. Feng, Z. Wei, P. Zhang, and X. Yuan, "Code-division OFDM joint communication and sensing system for 6G machine-type communication," *IEEE Internet Things J.*, vol. 8, no. 15, pp. 12 093–12 105, 2021.

[9] M. Bică and V. Koivunen, "Radar waveform optimization for target parameter estimation in cooperative radar-communications systems," *IEEE Trans. Aerosp. Electron. Syst.*, vol. 55, no. 5, pp. 2314–2326, 2019.

[10] C. Shi, F. Wang, M. Sellathurai, J. Zhou, and S. Salous, "Power minimization-based robust OFDM radar waveform design for radar and communication systems in coexistence," *IEEE Trans. Signal Process.*, vol. 66, no. 5, pp. 1316–1330, 2018.

[11] Y. Liu, G. Liao, J. Xu, Z. Yang, and Y. Zhang, "Adaptive OFDM integrated radar and communications waveform design based on information theory," *IEEE Commun. Lett.*, vol. 21, no. 10, pp. 2174–2177, 2017.

[12] Y. Liu, G. Liao, Z. Yang, and J. Xu, "Multiobjective optimal waveform design for OFDM integrated radar and communication systems," *Signal Process.*, vol. 141, pp. 331–342, 2017. [Online]. Available: https://www.sciencedirect.com/science/article/pii/S0165168417302360

[13] P. Kumari, S. A. Vorobyov, and R. W. Heath, "Adaptive virtual waveform design for millimeter-wave joint communication–radar," *IEEE Trans. Signal Process.*, vol. 68, pp. 715–730, 2020.

[14] S. M. Patole, M. Torlak, D. Wang, and M. Ali, "Automotive radars: A review of signal processing techniques," *IEEE Signal Process. Mag.*, vol. 34, no. 2, pp. 22–35, 2017.

[15] L. Li, K. Josiam, and R. Taori, "Feasibility study on full-duplex wireless millimeter-wave systems," in *Proc. IEEE Int. Conf. Acoust., Speech Signal Process. (ICASSP)*, 2014, pp. 2769–2773.

[16] S. Rajagopal, R. Taori, and S. Abu-Surra, "Self-interference mitigation for in-band mmWave wireless backhaul," in *Proc. IEEE Consum. Commun.Netw. Conf.*, 2014, pp. 551–556.

[17] W. M. Gifford, D. Dardari, and M. Z. Win, "The impact of multipath information on time-of-arrival estimation," *IEEE Trans. Signal Process.*, vol. 70, pp. 31–46, 2022.

[18] S. Wang, G. Mao, and J. A. Zhang, "Joint time-of-arrival estimation for coherent UWB ranging in multipath environment with multi-user interference," *IEEE Trans. Signal Process.*, vol. 67, no. 14, pp. 3743–3755, 2019.

[19] Y.-Y. Chen, S.-P. Huang, T.-W. Wu, W.-T. Tsai, C.-Y. Liou, and S.-G. Mao, "UWB system for indoor positioning and tracking with arbitrary target orientation, optimal anchor location, and adaptive NLoS mitigation," *IEEE Trans. Veh. Technol.*, vol. 69, no. 9, pp. 9304–9314, 2020.

[20] K. Yu, K. Wen, Y. Li, S. Zhang, and K. Zhang, "A novel NLoS mitigation algorithm for UWB localization in harsh indoor environments," *IEEE Trans. Veh. Technol.*, vol. 68, no. 1, pp. 686–699, 2019.

[21] C. Wang, J. Tian, J. Cao, and X. Wang, "Deep learning-based UAV detection in pulse-Doppler radar," *IEEE Trans. Geosci. Remote Sens.*, vol. 60, pp. 1–12, 2022.

[22] T. Ding, J. Zhang, S. Tang, L. Zhang, and Y. Li, "A novel iterative inner-pulse integration target detection method for bistatic radar," *IEEE Trans. Geosci. Remote Sens.*, vol. 60, pp. 1–15, 2022.

[23] Y. Song, J. Hu, N. Chu, T. Jin, J. Zhang, and Z. Zhou, "Building layout reconstruction in concealed human target sensing via UWB MIMO through-wall imaging radar," *IEEE Geosci. Remote Sens. Lett.*, vol. 15, no. 8, pp. 1199–1203, 2018.

[24] M. Setsu, T. Hayashi, J. He, and S. Kidera, "Super-resolution Doppler velocity estimation by kernel-based range–τ point conversions for UWB short-range radars," *IEEE Trans. Geosci. Remote Sens.*, vol. 58, no. 4, pp. 2430–2443, 2020.

[25] W. Shao, A. Edalati, T. R. McCollough, and W. J. McCollough, "A time-domain measurement system for UWB microwave imaging," *IEEE Trans. Microw. Theory Techn.*, vol. 66, no. 5, pp. 2265–2275, 2018.

[26] R. Feghhi, R. S. C. Winter, F. M. Sabzevari, and K. Rambabu, "Design of a low-cost UWB time-domain radar system for subcentimeter image resolution," *IEEE Trans. Microw. Theory Techn.*, vol. 70, no. 7, pp. 3617–3628, 2022.

[27] T. I. Krébesz, G. Kolumbán, C. K. Tse, F. C. M. Lau, and H. Dong, "Use of UWB impulse radio technology in in-car communications: Power limits and optimization," *IEEE Trans. Veh. Technol.*, vol. 66, no. 7, pp. 6037–6049, 2017.

[28] X. Cheng and Y. L. Guan, "Narrow-band interference suppression in impulse-radio ultrawideband systems," *IEEE Trans. Veh. Technol.*, vol. 63, no. 7, pp. 3440–3446, 2014.

[29] S. Sharma, A. Gupta, and V. Bhatia, "Impulse noise mitigation in IR-UWB communication using signal cluster sparsity," *IEEE Commun. Lett.*, vol. 22, no. 3, pp. 558–561, 2018.

[30] S. Aldirmaz-Colak, E. Aydin, Y. Celik, Y. Acar, and E. Basar, "Pulse index modulation," *IEEE Commun. Lett.*, vol. 25, no. 7, pp. 2309–2313, 2021.

[31] A. Maali, A. Boukhelifa, A. Mesloub, S. Sadoudi, and M. Benssalah, "An enhanced pulse position modulation (PPM) for both IR-UWB and DCC-UWB communication," in *Proc. Eur. Conf. Antennas Propag. (EuCAP)*, 2019, pp. 1–5.

[32] S. Sharma and Y. Hong, "UWB receiver via deep learning in MUI and ISI scenarios," *IEEE Trans. Veh. Technol.*, vol. 69, no. 3, pp. 3496–3499, 2020.

[33] L. Chen, Z. Wang, Y. Du, Y. Chen, and F. R. Yu, "Generalized transceiver beamforming for DFRC with MIMO radar and MU-MIMO communication," *IEEE J. Sel. Areas Commun.*, vol. 40, no. 6, pp. 1795–1808, 2022.

[34] L. Chen, F. Liu, W. Wang, and C. Masouros, "Joint radar-communication transmission: A generalized pareto optimization framework," *IEEE Trans. Signal Process.*, vol. 69, pp. 2752–2765, 2021.

[35] F. Liu, C. Masouros, A. Li, H. Sun, and L. Hanzo, "MU-MIMO communications with MIMO radar: From co-existence to joint transmission," *IEEE Trans. Wireless Commun.*, vol. 17, no. 4, pp. 2755–2770, 2018.

[36] F. Liu, L. Zhou, C. Masouros, A. Li, W. Luo, and A. Petropulu, "Toward dual-functional radar-communication systems: Optimal waveform design," *IEEE Trans. Signal Process.*, vol. 66, no. 16, pp. 4264–4279, 2018.

[37] M. Win and R. Scholtz, "On the energy capture of ultrawide bandwidth signals in dense multipath environments," *IEEE Commun. Lett.*, vol. 2, no. 9, pp. 245–247, 1998.

[38] A. A. D'Amico, U. Mengali, and L. Taponecco, "ToA estimation with the IEEE 802.15.4a standard," *IEEE Trans. Wireless Commun.*, vol. 9, no. 7, pp. 2238–2247, 2010.

[39] D. Dardari, C.-C. Chong, and M. Win, "Threshold-based time-of-arrival estimators in UWB dense multipath channels," *IEEE Trans. Commun.*, vol. 56, no. 8, pp. 1366–1378, 2008.

[40] I. Guvenc, Z. Sahinoglu, and P. Orlik, "ToA estimation for IR-UWB systems with different transceiver types," *IEEE Trans. Microw. Theory Techn.*, vol. 54, no. 4, pp. 1876–1886, 2006.

[41] S. Sharma, V. Bhatia, and A. Gupta, "Joint symbol and ToA estimation for iterative transmitted reference pulse cluster UWB system," *IEEE Syst. J.*, vol. 13, no. 3, pp. 2629–2640, 2019.

[42] V. Yajnanarayana and P. Händel, "Joint estimation of ToA and PPM symbols using sub-Nyquist sampled IR-UWB signal," *IEEE Commun. Lett.*, vol. 21, no. 4, pp. 949–952, 2017.

[43] S. Sharma, V. Bhatia, and A. Gupta, "An iterative transmitted reference UWB receiver for joint ToA and data symbols estimation," in *Proc. IEEE Int Conf Commun*, 2018, pp. 1–7.

[44] A. Rabbachin, I. Oppermann, and B. Denis, "GML ToA estimation based on low complexity UWB energy detection," in *Proc. IEEE Int. Symp. Person., Indoor Mobile Radio Commun. (PIMRC)*, 2006, pp. 1–5.

[45] J.-Y. Lee and R. Scholtz, "Ranging in a dense multipath environment using an UWB radio link," *IEEE J. Sel. Areas Commun.*, vol. 20, no. 9, pp. 1677–1683, 2002.

[46] R. Walden, "Analog-to-digital converter survey and analysis," *IEEE J. Sel. Areas Commun.*, vol. 17, no. 4, pp. 539–550, 1999.

[47] F. Sun, H. Yin, and W. Wang, "Finite-resolution digital receiver for UWB ToA estimation," *IEEE Commun. Lett.*, vol. 16, no. 1, pp. 76–79, 2012.

[48] H. Yin, Z. Wang, L. Ke, and J. Wang, "Monobit digital receivers: design, performance, and application to impulse radio," *IEEE Trans. Commun.*, vol. 58, no. 6, pp. 1695–1704, 2010.

[49] F. Sun, H. Yin, and W. Wang, "Bounds on performance of UWB ToA estimation using finite resolution quantization," in *Proc. IEEE Wireless Commun. Networking Conf. (WCNC)*, 2013, pp. 2579–2584.

[50] N. J. Myers and R. W. Heath, "Message passing-based joint CFO and channel estimation in mmWave systems with one-bit ADCs," *IEEE Trans. Wireless Commun.*, vol. 18, no. 6, pp. 3064–3077, 2019.

[51] Y.-S. Jeon, N. Lee, S.-N. Hong, and R. W. Heath, "One-bit sphere decoding for uplink massive MIMO systems with one-bit ADCs," *IEEE Trans. Wireless Commun.*, vol. 17, no. 7, pp. 4509–4521, 2018.

[52] D. Neirynck, E. Luk, and M. McLaughlin, "An alternative double-sided two-way ranging method," in *Proc. Workshop Position., Navig. Commun. (WPNC)*, 2016, pp. 1–4.

[53] S. Gezici, Z. Tian, G. Giannakis, H. Kobayashi, A. Molisch, H. Poor, and Z. Sahinoglu, "Localization via ultra-wideband radios: a look at positioning aspects for future sensor networks," *IEEE Signal Process. Mag.*, vol. 22, no. 4, pp. 70–84, 2005.

[54] Y. Zhang, J. Ren, and W. Chen, "A ToA-based location algorithm reducing the NLoS error under location-aware networks," in *Proc. 7th Int. Conf. Wirel. Commun., Networking Mob. Comput. (WiCOM)*, 2011, pp. 1–4.

[55] T. Wang, K. Hu, Z. Li, K. Lin, J. Wang, and Y. Shen, "A semi-supervised learning approach for UWB ranging error mitigation," *IEEE Wireless Commun. Lett.*, vol. 10, no. 3, pp. 688–691, 2021.

[56] S. M. Kay, *Fundamentals of statistical processing, Volume 2: Detection theory*. Pearson Education India, 2009.

[57] H. K. Khalil, *Nonlinear systems third edition*. Prentice Hall, 2002.

[58] J. Foerster, "Channel modeling sub-committee report final," *IEEE P802. 15 Working Group for Wireless Personal Area Networks (WPANs)*, 2003.

[59] M. Win and R. Scholtz, "Ultra-wide bandwidth time-hopping spread-spectrum impulse radio for wireless multiple-access communications," *IEEE Trans. Commun.*, vol. 48, no. 4, pp. 679–689, 2000.

[60] "IEEE standard for low-rate wireless networks–amendment 1: Enhanced ultra wideband (UWB) physical layers (PHYs) and associated ranging techniques," *IEEE Std 802.15.4z-2020 (Amendment to IEEE Std 802.15.4-2020)*, pp. 1–174, 2020.

[61] C. Zhang, H. Yin, and P. Ren, "The effects of narrowband interference on finite-resolution IR-UWB digital receivers," *IEEE Commun. Lett.*, vol. 15, no. 5, pp. 536–538, 2011.

[62] M. Chiani and A. Giorgetti, "Coexistence between UWB and narrow-band wireless communication systems," *Proc. IEEE*, vol. 97, no. 2, pp. 231–254, 2009.

[63] S. T. B. News and S. T. B. News, *Detection, Estimation And Modulation Theory*. New York: wiley, 1968.

[64] S. M. Kay, "Fundamentals of statistical signal processing," *Technometrics*, vol. 37, no. 4, pp. 465–466, 1993.

[65] L. Ke, H. Yin, W. Gong, and Z. Wang, "Finite-resolution digital receiver design for impulse radio ultra-wideband communication," *IEEE Trans. Wireless Commun.*, vol. 7, no. 12, pp. 5108–5117, 2008.

[66] J. P. Romano and M. Wolf, "A more general central limit theorem for m-dependent random variables with unbounded m," *Stat. Probabil. Lett.*, vol. 47, no. 2, pp. 115–124, 2000.

[67] K. N. Berk, "A central limit theorem for m-dependent random variables with unbounded m," *Ann. Probab.*, pp. 352–354, 1973.

Shusen Cai received the B.E. degree in communications engineering from Xidian University, Xi'an, China, in 2020. He is currently pursuing the Ph.D. degree with the Department of Electronic Engineering and Information Science, University of Science and Technology of China. His research interests include low-resolution quantization, and integrated sensing and communication.
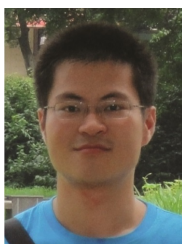
Li Chen (Senior Member, IEEE) received the B.E. in electrical and information engineering from Harbin Institute of Technology, Harbin, China, in 2009 and the Ph.D. degree in electrical engineering from the University of Science and Technology of China, Hefei, China, in 2014. He is currently an Associate Professor with the Department of Electronic Engineering and Information Science, University of Science and Technology of China. His research interests include integrated communication and computation, integrated sensing and communication and wireless IoT networks.
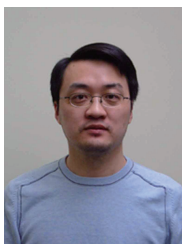
Yunfei Chen (S'02-M'06-SM'10) received his B.E. and M.E. degrees in electronics engineering from Shanghai Jiaotong University, Shanghai, P.R.China, in 1998 and 2001, respectively. He received his Ph.D. degree from the University of Alberta in 2006.He is currently a Professor with the Department of Engineering, University of Durham, U.K. His research interests include wireless communications, cognitive radios, wireless relaying and energy harvesting.

Huarui Yin (M'08) received the bachelor's degree and the Ph.D. degree in electronic engineering and information science from the University of Science and Technology of China (USTC), Hefei, Anhui, in 1996 and 2006, respectively. Since 2010, he has been with the Department of Electronic Engineering and Information Science, USTC, as an Associate Professor. His research interests include digital signal processing, low complexity receiver design, multiple access for massive connections, and throughput analysis of wireless networks.

Weidong Wang received the B.S. degree from Beijing University of Aeronautics and Astronautics, Beijing, China, in 1989 and the M.S. degree from the University of Science and Technology of China, Hefei, China, in 1993. He is currently a Full Professor with the Department of Electronic Engineering and Information Systems, University of Science and Technology of China. Prof. Wang is a member of the Committee of Optoelectronic Technology, Chinese Society of Astronautics. His research interests include wireless communication, microwave and millimeter-wave, and radar technology.